UNIVERSIDADE ESTADUAL DE CAMPINAS

Faculdade de Engenharia Mecânica

Brener d'Lelis Oliveira Ramos

High-Fidelity Simulation and Flow Control of a Plunging Airfoil under Deep Dynamic Stall

Simulação de Alta Fidelidade e Controle do Escoamento sobre um Aerofólio em Movimento de Plunge com Estol Dinâmico Profundo

CAMPINAS

2019

Brener d'Lelis Oliveira Ramos

High-Fidelity Simulation and Flow Control of a Plunging Airfoil under Deep Dynamic Stall

Simulação de Alta Fidelidade e Controle do Escoamento sobre um Aerofólio em Movimento de Plunge com Estol Dinâmico Profundo

Dissertation presented to the School of Mechanical Engineering of the University of Campinas in partial fulfillment of the requirements for the degree of Master in Mechanical Engineering, in the area of Thermal and Fluids.

Dissertação apresentada à Faculdade de Engenharia Mecânica da Universidade Estadual de Campinas como parte dos requisitos exigidos para a obtenção do título de Mestre em Engenharia Mecânica, na Área de Térmica e Fluidos.

Orientador: William Roberto Wolf

Este exemplar corresponde à versão final da dissertação defendida pelo aluno Brener d'Lelis Oliveira Ramos, e orientada pelo Prof. Dr. William Roberto Wolf.

Assinatura do Orientador

_____

Campinas

2019

Ficha catalográfica
Universidade Estadual de Campinas
Biblioteca da Área de Engenharia e Arquitetura
Luciana Pietrosanto Milla - CRB 8/8129

R147h

Ramos, Brener d'Lelis Oliveira, 1993-
High-fidelity simulation and flow control of a plunging airfoil under deep dynamic stall / Brener d'Lélis Oliveira Ramos. – Campinas, SP : [s.n.], 2019.

Orientador: William Roberto Wolf.
Dissertação (mestrado) – Universidade Estadual de Campinas, Faculdade de Engenharia Mecânica.

1. Fluidodinâmica computacional (CFD). I. Wolf, William Roberto, 1980-. II. Universidade Estadual de Campinas. Faculdade de Engenharia Mecânica. III. Título.

Informações para Biblioteca Digital

Título em outro idioma: Simulação de alta fidelidade e controle do escoamento sobre um aerofólio em movimento de plunge com estol dinâmico profundo
Palavras-chave em inglês:
Computational fluid dynamics (CFD)
Área de concentração: Térmica e Fluídos
Titulação: Mestre em Engenharia Mecânica
Banca examinadora:
William Roberto Wolf [Orientador]
Kunihiko Taira
Flávio Donizeti Marques
Data de defesa: 19-08-2019
Programa de Pós-Graduação: Engenharia Mecânica

Identificação e informações acadêmicas do(a) aluno(a)
- ORCID do autor: https://orcid.org/0000-0002-6325-5647
- Currículo Lattes do autor: http://lattes.cnpq.br/6410963126327398

UNIVERSIDADE ESTADUAL DE CAMPINAS

FACULDADE DE ENGENHARIA MECÂNICA

COMISSÃO DE PÓS-GRADUAÇÃO EM ENGENHARIA MECÂNICA

DEPARTAMENTO DE TÉRMICA E FLUIDOS

DISSERTAÇÃO DE MESTRADO ACADÊMICO

High-Fidelity Simulation and Flow Control of a Plunging Airfoil under Deep Dynamic Stall

Simulação de Alta Fidelidade e Controle do Escoamento sobre um Aerofólio em Movimento de Plunge com Estol Dinâmico Profundo

Autor: Brener d'Lelis Oliveira Ramos

Orientador: William Roberto Wolf

A Banca Examinadora composta pelos membros abaixo aprovou esta dissertação:

Prof. Dr. William Roberto Wolf - Presidente FEM/UNICAMP

Prof. Dr. Flávio Donizeti Marques - Universidade de São Paulo, São Carlos

Prof. Dr. Kunihiko Taira - University of California, Los Angeles

A Ata da defesa com as respectivas assinaturas dos membros encontra-se no processo de vida acadêmica do aluno.

Campinas, 19 de Agosto de 2019.

This work is dedicated to everyone who supported me since the beginning of this journey and specially my advisor, my family and my girlfriend. Without this support none of this would be possible.

"A man without dreams is a dead man.", C. Lélis

Acknowledgments

I am grateful for all insights and help provided by all my labmates at Unicamp. Two years ago I barely knew how to open a terminal and they were responsible for helping me figure uncountable things. I also want to thank my labmates during my stay at Tallahassee. They were really kind and helped me a lot to get settled in the new town. I am very appreciated for all the support and advices from Dr. Kunihiko Taira and Dr. Chi-An Yeh. It was a great experience to work alongside them for six months.

I want to thank Dr. Flávio Marques for participating in the committee of this thesis since the qualification stages. I really appreciate all the help and support given by Dr. William Wolf, which I have been working with since 2014, and my family, who always believed in me. Last but not least, I am very grateful for all incentive I have been receiving for years from Ana Paula, who never doubted me.

I want to acknowledge the financial support received from FAPESP, under Grants No. 2013/07375-0, 2016/24504-6, 2018/04210-3 and CAPES. I also thank CENAPAD-SP (Project 551), SDUMONT-LNCC and CEPID-CeMEAI for providing the computational resources for this work.

Resumo

Simulações de alta fidelidade são realizadas com o intuito de estudar técnicas de controle ativo para amenizar um vórtice de estol dinâmico em um aeorfólio SD7003 em manobra de *plunge* com número de Reynolds Re = 60000 e número de Mach M = 0,1. Simulações numéricas são realizadas utilizando uma ferramenta numérica que incorpora métodos compactos de alta ordem para diferenciação, interpolação e filtragem numa malha deslocada. Um estudo de convergência de malha é conduzido e os resultados obtidos mostram boa concordância com dados disponíveis na literatura em termos de coeficientes aerodinâmicos. Atuadores com diferentes arranjos na direção da envergadura foram modelados afim de simular o assopramento e sucção do escoamento na região do bordo de ataque. Foi observado que, numa faixa de frequências específica, a média e flutuação de arrasto foram subtancialmente reduzidas enquanto a sustentação quase não foi afetada, especialmente para um atuador bi-dimensional (2D). Nessa faixa de frequências, atuação 2D perturba a formação do vórtice de estol dinâmico, o que leva a uma redução do arrasto devido ao aumento da pressão no extradorso do aerofólio na região de meia corda. Ao mesmo tempo, a pressão é reduzida na proximidade do bordo de ataque, o que aumenta sustentação e empuxo. Uma decomposição modal do escoamento também é realizada. Com apenas 20 modos da decomposição, notou-se que a maior parte da dinâmica do escoamento responsável pelos coeficientes aerodinâmicos é recuperada.

Palavras-chave: controle de escoamento, estol dinâmico, decomposição modal, dinâmica dos fluidos computacional

Abstract

High-fidelity simulations are performed to study active flow control techniques for alleviating deep dynamic stall of a SD7003 airfoil in a plunging motion at Reynolds number Re = 60,000 and freestream Mach number M = 0.1. Numerical simulations are performed with a finite difference based solver that incorporates high-order compact schemes for differentiation, interpolation and filtering on a staggered grid. A mesh convergence study is conducted and results show good agreement with available data in terms of aerodynamic coefficients. Different spanwise arrangements of actuators are implemented to simulate blowing and suction at the airfoil leading edge. It is observed that, for a specific frequency range of actuation, mean drag and drag fluctuations are substantially reduced while mean lift is maintained almost unaffected, especially for a 2D actuator setup. At this frequency range, 2D flow actuation disrupts the formation of the dynamic stall vortex, what leads to drag reduction due to a pressure increase along the airfoil suction side, towards the trailing edge region. At the same time, pressure is reduced near the leading edge, increasing both lift and thrust. Modal decomposition is then performed and it is found that, with only 20 modes, most of the flow dynamics responsible for the aerodynamic loads is recovered.

Keywords: flow control, dynamic stall, modal decomposition, computational fluid dynamics

List of Figures

List of Tables

List of Acronyms

Latin characters

$\vec{a}$	-	POD/SPOD temporal modes
C_D	-	Drag coefficient
C_f	-	Skin friction coefficient
C_L	-	Lift coefficient
C_M	-	Momentum coefficient
C_P	-	Pressure coefficient
C_μ	-	Coefficient of transferred momentum
$\frac{\overline{C_L}}{\overline{C_D}}$	-	Mean lift relative to mean drag
E	-	Energy density
g	-	Metric terms
h	-	Function that describes plunge motion
h_o	-	Amplitude of plunge motion
k	-	Reduced frequency of plunge motion
M	-	Mach number
n	-	Number of snapshots
n_f	-	Bandwidth size of SPOD filter
p	-	Pressure
Pr	-	Prandtl number
q	-	Coefficients of SPOD filter
R	-	Correlation matrix
Re	-	Reynolds number
S	-	Filtered correlation matrix
St	-	Strouhal number
T	-	Temperature
t	-	Time
u	-	Velocity
U_{jet}	-	Velocity of actuation jet
$U_{jet\,max}$	-	Maximum velocity of actuation jet
U_∞	-	Freestream velocity

Greek characters

α	-	Angle of attack
γ	-	Ratio of specific heats
Δz	-	Spanwise width of actuator
λ	-	Singular value
μ	-	Viscosity
ξ	-	Curvilinear coordinates
Ξ	-	Aerodynamic damping
ρ	-	Density
τ	-	Stress tensor
ϕ	-	Phase Angle
Ψ	-	POD/SPOD spatial modes
ω_z	-	Z-vorticity

Other symbols

$\left\{ {i \atop jk} \right\}$	-	Chrsitoffel symbol

Abbreviations

2D	-	Two-dimensional
3D	-	Three-dimensional
FFT	-	Fast Fourier Transform
POD	-	Proper Orthogonal Decomposition
SPOD	-	Spectral Proper Orthogonal Decomposition

Contents

1 Introduction

Aerodynamic bodies moving through steady and unsteady flows are found in several engineering applications. Examples include helicopter rotor blades, wind turbine blades, maneuvering aircraft, unmanned air vehicles (UAVs), to name a few. In general, airfoil motion can be modeled by pitching and plunging, or combinations of both. The latter can lead, for example, to the Knoller-Betz or Katzmayr effect (Jones *et. al*, 1998), where a sinusoidally plunging airfoil can produce thrust depending on specific flow parameters such as motion frequency and amplitude. Pitching is described by a pure rotation of the airfoil, usually at quarter chord from the leading edge, while plunging is represented its pure vertical translation. Despite not having rotation, an airfoil in plunging motion experiences a change in effective angle of attack, which is that between the airfoil chord and the effective disturbed flow velocity.

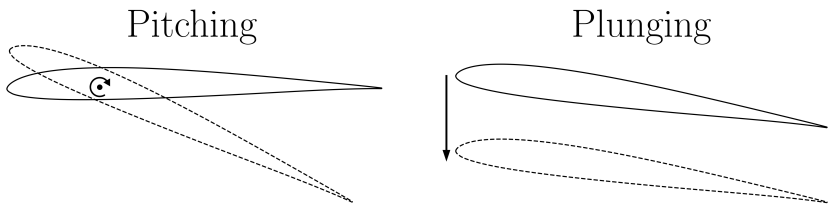

Figure 1.1: Schematic of airfoil pitching and plunging motions.

Unsteady flows over plunging and pitching airfoils with large excursions in effective angle of attack exhibit the phenomenon of dynamic stall. This process is characterized by unsteady separation and formation of a large leading-edge vortex, also called dynamic stall vortex, that exerts high amplitude fluctuations in the aerodynamic loads. Comprehensive reviews of this phenomenon in the context of helicopter rotor blades and pitching airfoils are provided by McCroskey (1982); Carr (1988); Ekaterinaris and Platzer (1998) and Corke and Thomas (2015).

A brief schematic showing how the dynamic stall phenomenon of a pitching airfoil takes place can be seen in Fig. 1.2. At the start of the pitch-up motion in the cycle (stage 1 in Fig. 1.2), the boundary layer is attached on the suction side of the airfoil and lift increases linearly with pitch angle. This continues until the airfoil reaches its static stall angle of attack. Lift then continues to increase beyond that angle as a result of two mechanisms: i) a delay in the boundary layer separation owing to the pitching motion and ii) formation of a separation bubble near the airfoil leading edge. Stage 2

of the flow corresponds to the first appearance and subsequent growth of the dynamic stall vortex. This involves the spontaneous generation and ejection of vorticity from the boundary layer into the inviscid outer flow, in a process detailed by Dommelen and Shen (1980). The growth of the dynamic stall vortex results in additional aerodynamic loading that exceeds that of the steady airfoil. In the same figure, one can see the advection of the dynamic stall vortex at stage 3. At later stages, the flow becomes massively separated and is later re-attached during the pitch-down motion.

For the case of flapping wings, as well as for severe impinging gusts, Eldredge and Jones (2019) showed that highly unsteady forcing induces the formation of dynamic stall. The evolution and interaction of such vortical structures with aerodynamic surfaces have a significant impact on flight stability and performance. At certain conditions, dynamic stall can lead to negative damping, which means that energy is being transferred from the flow to the aerodynamic body, resulting in the growth of oscillations. This phenomenon is referred to as stall flutter and can lead to catastrophic mechanical failure as showed by Ham and Young (1966).

Although several studies have been conducted for pitching airfoils at high Reynolds numbers, research on dynamic stall for plunging airfoils is more scarce, especially at low and moderate Reynolds numbers. Studies of airfoils with plunging motion in these conditions find application in design and operation of small unmanned air vehicles and micro air vehicles. Therefore, we aim to extend our knowledge on the flow features present in fully separated low Reynolds number flows involving deep dynamic stall.

High-fidelity simulations can provide an abundance of data with both high spatial and temporal resolutions. For example, Ekaterinaris and Platzer (1998); Visbal and Shang (1989); Visbal (1991); Choudhuri *et. al* (1994); Visbal (1990) and Radespiel *et. al* (2007) performed two-dimensional simulations of dynamic stall under laminar, transitional, and turbulent flow conditions. For high Reynolds number flows, numerical simulations traditionally employ a hierarchy of turbulence models augmented in some instances with empirical transition predictions. Over the last years, Visbal and co-authors have employed implicit large eddy simulation (ILES) to investigate the phenomenon of dynamic stall for different flow configurations including plunging and pitching motion, as can be seen in Visbal (2011, 2014, 2015); Visbal and Garmann (2017); Benton and Visbal (2018) and Visbal and Benton (2018).

In the present work, implicit large eddy simulations are performed to study the flow physics of deep dynamic stall over a plunging SD7003 airfoil. The flow condition investigated is selected based on the availability of results from other high fidelity simulations by Visbal (2011) and particle image velocimetry (PIV) by Kang *et. al* (2009);

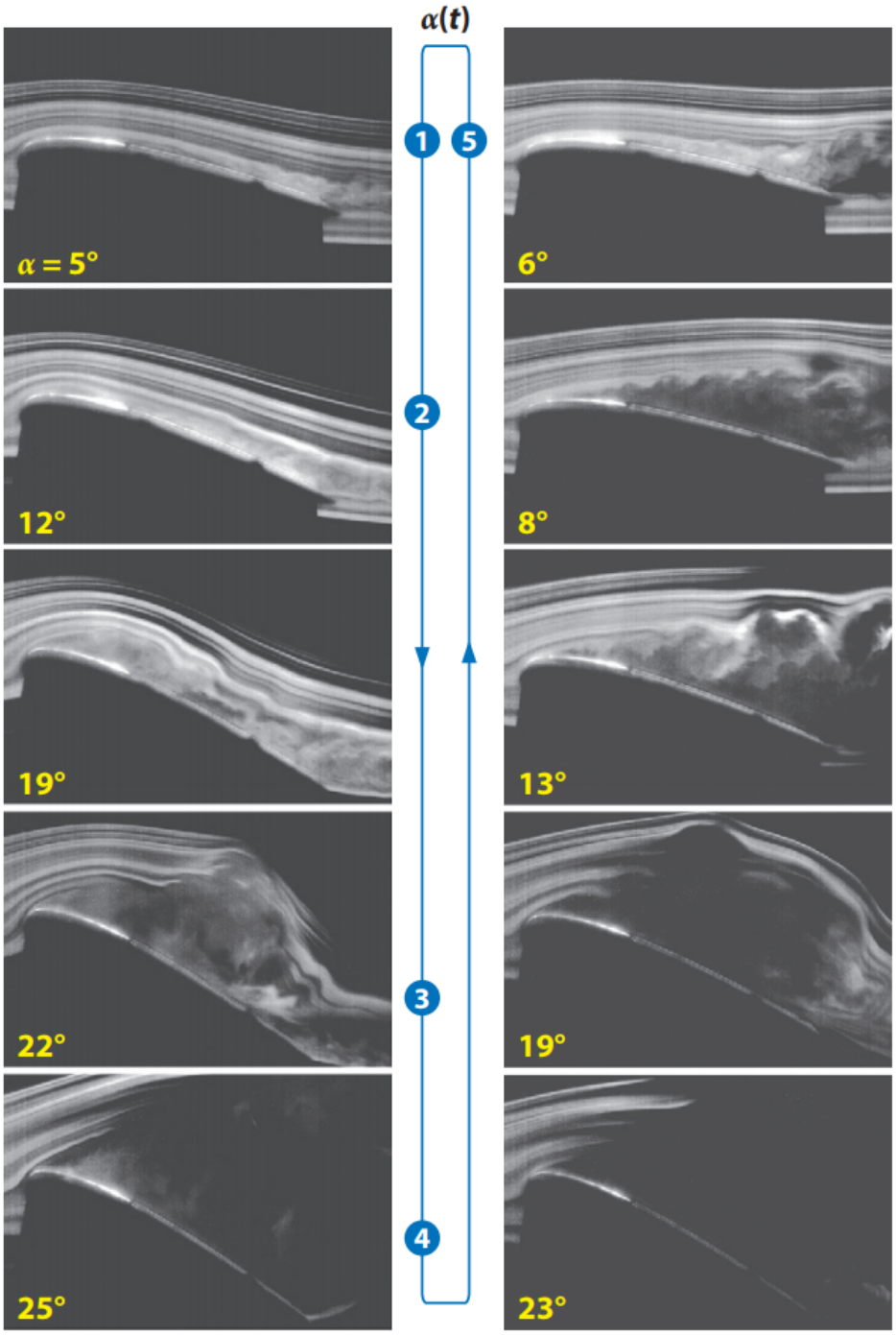

Figure 1.2: Experiment showing how the flow is modified by a pitching airfoil at different angles of attack. Extracted from Corke *et. al* (2011).

Baik *et. al* (2009); Ol *et. al* (2009). A compressible formulation is adopted since local Mach numbers near the leading edge of a moving airfoil can be three to five times higher than in static condition, as demonstrated by McCroskey (1981) and McCroskey (1982). As a result, compressibility effects must be taken into consideration even for low Mach

number flows.

Several investigations of dynamic stall control by both active and passive means, especially for pitching airfoils, are described in the survey by Lorber *et. al* (2000). Different control strategies have been tested including leading-edge blowing by Greenblatt and Wygnanski (2001); Sun and Sheikh (1999); Weaver *et. al* (2004), leading-edge plasma actuation by Corke *et. al* (2011); Lombardi *et. al* (2013); Post and Corke (2006), thermo-acoustic actuation by Benton and Visbal (2018), vortex generators by Heine *et. al* (2013); Martin *et. al* (2008); Traub *et. al* (2004) and synthetic jets by Ekaterinaris (2002); Florea and Wake (2003); Traub *et. al* (2004). In some cases, fixed-wing devices have been used, such as slots used by Carr *et. al* (2001), leading-edge droops by Chandrasekhara *et. al* (2004); Joo *et. al* (2006); Martin *et. al* (2008) and trailing-edge flaps by Feszty *et. al* (2004); Gerontakos and Lee (2006).

In this work, blowing and suction actuation is modeled at the airfoil leading-edge aiming to reduce overall drag through modification of the dynamic stall vortex. Active flow control strategies by means of periodic forcing can have effects such as attaching otherwise separated flows or avoiding separation, and increasing lift, as demonstrated by Greenblatt *et. al* (2010). Previous works by Visbal (2014, 2015); Visbal and Garmann (2017) show that small disturbances can have a considerable impact on the flow dynamics for a pitching NACA0012 experiencing dynamic stall at high Reynolds numbers. In the current investigation, it is shown that, for a specific frequency range of actuation, drag is substantially reduced while lift is maintained almost unaffected. The physical mechanisms responsible for the changes in the flow field achieved by actuation are then discussed.

Flow modal decomposition utilizing proper orthogonal decomposition (POD) and spectral proper orthogonal decomposition (SPOD) is also performed to both non-actuated and actuated flows. Those techniques extract modes based on optimizing the mean square of the field variable being examined. The modes extracted can be used to identify coherent structures in the turbulent flow field and, thus, aiding in the understanding of the fluid dynamics taking place. It is found that with only 20 modes, most of the dynamics impacting the aerodynamic coefficients is recovered. Also, from this latter study, it was possible to identify coherent structures originated from actuation.

1.1 Objectives

The main objective of this work is to investigate the phenomenon of deep dynamic stall of an airfoil under plunging motion. In order to perform this study, a tool

capable of simulating turbulent flows past moving bodies was developed. Hence, a computational fluid dynamics code available in the research group was extended to solve the three-dimensional form of the Navier-Stokes equations in a non-inertial frame of reference. This previous tool could already solve two-dimensional flows of aerodynamic bodies in arbitrary motion. Another objective of the current work consisted in performing implicit large eddy simulations of a plunging airfoil using high order methods. These simulations require a considerable amount of computational resources including parallel processing and storage, and improvements in the code structure and format of solution files were made to optimize the numerical procedure. Once the previous objectives were achieved, another main goal of the work consisted in the investigation of flow actuation effects on mitigation of the dynamic stall vortex in the studied flow. The flow actuation was performed through blowing and suction on the airfoil leading edge. Finally, another goal of this work was related to understanding how different actuation parameters, such as the amount of transferred momentum, actuator arrangement, and actuation frequency could impact flow parameters as drag and lift, besides the aerodynamic damping.

1.2 Work Organization

The layout of this MSc dissertation is organized as follows: chapter 2 describes the theoretical and numerical methodologies of the simulations conducted along this work. It is explained how the Navier-Stokes equations are solved in non-inertial frame of reference, and how differentiation, interpolation, filtering and time integration of the governing equations are performed. Details of the blowing and suction actuator is also provided including its modeling and implementation.

In chapter 3, details about overall flow configuration are given and a mesh convergence study is performed to validate the present numerical framework. Flow features at various instants of the plunging motion of a non-actuated flow are detailed. Also, a comparison between airfoils under dynamic and static stall at similar effective angles of attack is provided at the end of this chapter.

The impact of actuation is investigated in chapter 4. Effects of different actuation frequencies, jet intensities and slot arrangements are compared and a detailed explanation on how actuation can mitigate the dynamic stall vortex is given. The impact of flow actuation is shown for aerodynamic coefficients and aerodynamic damping. Theoretical aspects of flow modal decomposition is then discussed followed by results in chapter 5. It is explained how the modal decomposition techniques are formulated, including their

differences when applied to the present flow simulation data. At last, main conclusions are drawn in chapter 6 together with suggestions for future work.

2 Theoretical and Numerical Methodology

2.1 Governing Equations

To simulate the flow around a moving airfoil, we solve the weakly conservative form of the Navier-Stokes equations in a non-inertial frame. In this form, source terms emerge from grid curvature and frame movement as investigated by Warsi *et. al* (1978); Yamamoto and Daiguji (2001); Orlandi (1989); Choi (1992), and Yang and Voke (2001). Here, all terms are solved in contravariant form to allow the use of a curvilinear coordinate system $\{\xi^1, \xi^2, \xi^3\}$. All equations are non-dimensionalized by freestream quantities such as density ρ_∞ and freestream speed of sound c_∞. Although the Navier-Stokes equations are non-dimensionalized by speed of sound, displayed results and parameters are provided non-dimensionalized with respect to freestream velocity U_∞ in accordance with Visbal (2011). All length scales are made non-dimensional by the airfoil chord L. For a frame of reference with varying velocity in the Cartesian y-direction, continuity, momentum and energy equations reduce to

$$\frac{\partial}{\partial t}(\sqrt{g}\rho) + \frac{\partial}{\partial \xi^i}(\sqrt{g}\rho u^i) = 0 \ , \tag{2.1}$$

$$\begin{aligned}\frac{\partial}{\partial t}(\sqrt{g}\rho u^i) + \frac{\partial}{\partial \xi^j}\left[\sqrt{g}\left(\rho u^i u^j - \tau^{ij} + g^{ij}p\right)\right] \\ + \begin{Bmatrix} i \\ jk \end{Bmatrix}\sqrt{g}\Big(\rho u^k u^j + g^{jk}p - \tau^{kj}\Big) = \sqrt{g}\rho\ddot{h}^i \ ,\end{aligned} \tag{2.2}$$

and

$$\begin{aligned}\frac{\partial}{\partial t}(\sqrt{g}E) + \frac{\partial}{\partial \xi^j}\Big\{\sqrt{g}\Big[(E+p)u^j - \tau^{ij}g_{ik}u^k \\ - \frac{\mu M}{Re\, Pr}g^{ij}\frac{\partial T}{\partial \xi^i}\Big]\Big\} = \rho\sqrt{g}(h^j + u^j)g_{jp}\ddot{h}^p \ .\end{aligned} \tag{2.3}$$

In order to close the above system of equations the following relations are employed

$$E = \frac{p}{\gamma - 1} + \frac{1}{2}\rho u^i g_{ij} u^j + \frac{1}{2}\rho \dot{h}^i g_{ij}\dot{h}^i \ , \tag{2.4}$$

$$\tau^{ij} = \frac{\mu M}{Re}\left(g^{jk}u^{i}{}_{|k} + g^{ik}u^{j}{}_{|k} - \frac{2}{3}g^{ij}u^{k}{}_{|k}\right) \ , \tag{2.5}$$

and

$$h = h_o \sin(kt) \ , \tag{2.6}$$

where, ρ represents the density, u^i the i-th component of the contravariant velocity vector and p is the pressure. The term h is the frame position (cross-stream motion of the plunging airfoil), E is the total energy, μ is the dynamic viscosity, T is the temperature, $k = \frac{2\pi f L}{U_\infty}$ is the reduced frequency, $Re = \frac{\rho U_\infty L}{\mu}$ is the chord-based Reynolds number, $M = \frac{U_\infty}{c_\infty}$ is the freestream Mach number and Pr is the Prandtl number. The dots represent temporal derivatives of the frame position, i.e., frame velocity and acceleration. In the previous equations, covariant and contravariant metric tensors are defined, respectively, as

$$g_{ij} \triangleq \frac{\partial x^k}{\partial \xi^i}\frac{\partial x^k}{\partial \xi^j} \ , \tag{2.7}$$

and

$$g^{ij} \triangleq \frac{\partial \xi^i}{\partial x^k}\frac{\partial \xi^j}{\partial x^k} \ , \tag{2.8}$$

with

$$g = |g_{ij}| = \left(\frac{\partial x^i}{\partial \xi^j}\right)^2 \ . \tag{2.9}$$

The terms $\left\{ {i \atop jk} \right\}$ represent the Christoffel symbols of the second kind and details about the present formulation can be found in Aris (1989).

2.2 Numerical Methods

2.2.1 Spatial Differentiation

A compact sixth-order finite-difference scheme constructed for a staggered grid is used to calculate all spatial derivatives. To determine f' for a given f, a tridiagonal system is solved as

$$\alpha f'_{i-1} + f'_i + \alpha f'_{i+1} = b\frac{f_{i+3/2} - f_{i-3/2}}{3\Delta x} + a\frac{f_{i+1/2} - f_{i-1/2}}{\Delta x} \ , \tag{2.10}$$

where $\alpha = 9/62$, $a = \frac{3}{8}(3 - 2\alpha)$ and $b = \frac{1}{8}(-1 + 22\alpha)$. To minimize errors from unresolved scales, a sixth-order compact low-pass filter is applied according to

$$\bar{\alpha}\bar{f}_{i-1} + \bar{f}_i + \bar{\alpha}\bar{f}_{i+1} = \bar{a}f_i + \frac{\bar{b}}{2}(f_{i+1} + f_{i-1}) + \frac{\bar{c}}{2}(f_{i+2} + f_{i-2}) + \frac{\bar{d}}{2}(f_{i+3} + f_{i-3}) \ , \tag{2.11}$$

where, $\bar{a} = \frac{1}{16}(11+10\bar{\alpha})$, $\bar{b} = \frac{1}{32}(15+34\bar{\alpha})$, $\bar{c} = \frac{1}{16}(-3+6\bar{\alpha})$ and $\bar{d} = \frac{1}{32}(1-2\bar{\alpha})$. In the current implicit large eddy simulations, we use $\bar{\alpha} = 0.46$, which implies a filter that only acts on poorly resolved high wavenumbers. Therefore, this filter provides a reliable alternative to a SGS model as discussed by Visbal and Benton (2018). Due to the staggered grid, interpolations are necessary to evaluate properties at specific grid locations. To maintain schemes with high-order, a sixth-order interpolation based on finite differences is used according to

$$\tilde{\alpha}\tilde{f}_{i-1} + \tilde{f}_i + \tilde{\alpha}\tilde{f}_{i+1} = \frac{\tilde{b}}{2}(f_{i+3/2} + f_{i-3/2}) + \frac{\tilde{a}}{2}(f_{i+1/2} + f_{i-1/2}) \ , \tag{2.12}$$

where $\tilde{\alpha} = 3/10$, $\tilde{a} = \frac{1}{8}(9+10\tilde{\alpha})$ and $\tilde{b} = \frac{1}{8}(6\tilde{\alpha}-1)$. Additional details on the finite-difference schemes used for derivation, filtering and interpolation can be found in Lele (1992) and Nagarajan (2004).

Near the far-field boundaries, a numerical sponge is used to damp acoustic waves. At the inlet and outlet boundaries, a Riemann invariant transformation is implemented as the far-field condition. The airfoil surface is modeled by a no-slip adiabatic wall. Derivatives of inviscid fluxes are obtained by forming fluxes between the grid nodes, on the staggered grid, and differentiating each component. Viscous terms are obtained by first computing the derivatives of primitive variables at their respective locations (see Nagarajan (2004) for details). Components of the viscous fluxes are then constructed at each node and differentiated by a second application of the compact scheme. Airfoil movement is added through source terms shown in the formulation section. All schemes discussed are implemented with periodic boundary conditions in the spanwise ξ^3 direction. Since we employ an O-grid, periodic conditions are also enforced along the ξ^1 direction, along the mesh branch cut, where grid points are coincident.

2.2.2 Time Integration

After the spatial discretization, the Navier-Stokes equations become a set of ordinary differential equations that can be expressed in the form

$$\frac{d\boldsymbol{Q}}{dt} = \boldsymbol{F}(\boldsymbol{Q}, t) \ , \tag{2.13}$$

where $\boldsymbol{Q}$ is the vector of flow variables. At flow regions far away from solid boundaries, an explicit third-order Runge-Kutta scheme is used for the equations time marching. This scheme is given by

$$\begin{aligned} \boldsymbol{Q}^{n+1/3} &= \boldsymbol{Q}^n + \frac{8}{15}\Delta t \boldsymbol{F}(\boldsymbol{Q}^n, t^n) \\ \boldsymbol{Q}^{n+2/3} &= \boldsymbol{Q}^n + \frac{1}{4}\Delta t \boldsymbol{F}(\boldsymbol{Q}^n, t^n) + \frac{5}{12}\Delta t \boldsymbol{F}(\boldsymbol{Q}^{n+1/3}, t^{n+1/3}) \\ \boldsymbol{Q}^{n+1} &= \boldsymbol{Q}^n + \frac{1}{4}\Delta t \boldsymbol{F}(\boldsymbol{Q}^n, t^n) + \frac{3}{4}\Delta t \boldsymbol{F}(\boldsymbol{Q}^{n+2/3}, t^{n+2/3}) \ , \end{aligned} \tag{2.14}$$

where the intermediate time levels are $t^{n+1/3} = t^n + (8/15)\Delta t$ and $t^{n+2/3} = t^n + (2/3)\Delta t$.

Time integration is carried out by the fully implicit second-order scheme of Beam and Warming (1978) in the near-wall region in order to overcome the time step restriction due to the usual near-wall fine-grid numerical stiffness. An overlap layer is applied at the interface between explicit and implicit time marching schemes so that information can travel between them. The implicit method is given by

$$\frac{3Q^{n+1} - 4Q^n + Q^{n-1}}{2\Delta t} = \boldsymbol{F}(\boldsymbol{Q}^{n+1}, t^{n+1}) \ . \tag{2.15}$$

The right hand side is solved through approximate factorization followed by diagonalization of the implicit matrix in the x and z directions. More details about the approximate factorization are presented by Nagarajan (2004). After each time-step of both schemes, the previously explained low-pass compact filter is applied.

2.3 Actuator Setup

In the current work, flow control is performed using blowing and suction on the leading edge of the airfoil. To simulate an actuator of length $s \approx 0.01L$, as shown in Fig. 2.1a, a normal velocity is imposed at the actuator location, which is centered around the airfoil

leading edge and is imposed with Eqs. (2.16) – (2.18) as

$$\frac{U_{jet}}{U_\infty} = \frac{U_{jet\,max}}{U_\infty} F(s)\, G(t)\, P(z) \quad \text{with} \tag{2.16}$$

$$F(s) = \exp\left(- \frac{(s^* - 0.01)^2}{4.5} \right), \quad s^* = 5(s - 0.005) \quad \text{and} \tag{2.17}$$

$$G(t) = \sin(St\, 2\pi t)\ , \tag{2.18}$$

where the Strouhal number is $St = \frac{fL}{U_\infty}$.

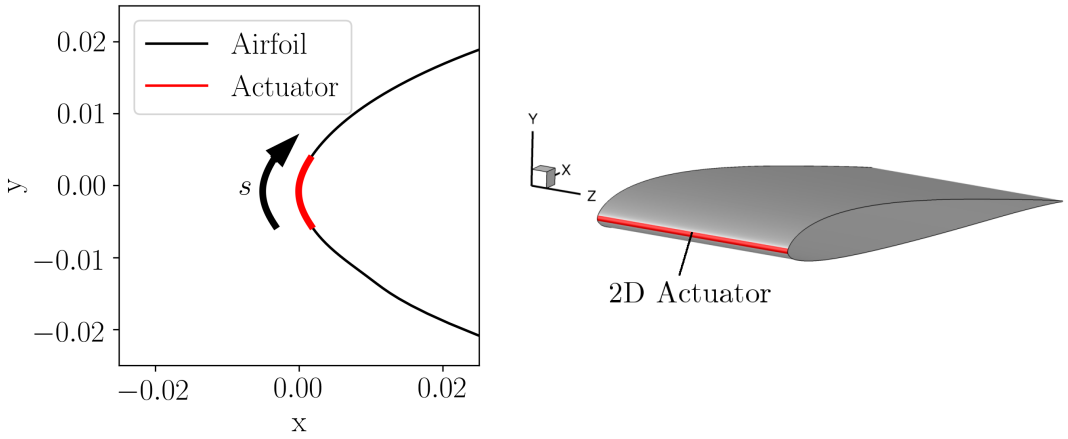

(a) (b)

Figure 2.1: (a) Actuator location in the x-y plane. (b) 3D view of 2D actuator.

The jet actuation is a sinusoidal temporal function $G(t)$ given by a Gaussian profile $F(s)$ along the wall-tangential direction s and a profile $P(z)$ along the airfoil span with maximum jet velocity set as $U_{jet\,max}$. The spanwise actuation functions are chosen with the intent of approximating the format of real slots on the airfoil surface. This would allow comparisons to experiments. We defined the actuator chordwise location after analyzing how efficiently the shear layer and overall flow are disturbed with different actuator positions. For a pitching airfoil, Benton and Visbal (2018) showed that an actuator placed near the leading edge effectively modifies the flow with minimum input.

To assess the influence of spanwise arrangement of actuation, different spanwise jet configurations are tested through modifications of function $P(z)$. A 2D actuator is analyzed setting $P(z) = 1$ (see Fig. 2.1b). Other configurations are obtained appending points according to

$$P_{actuator}(z) = \tanh\left(\frac{2(\beta - \alpha)}{\Delta z_{actuator}} z + \alpha \right) \frac{1}{2} + \frac{1}{2}, \quad 0 \le z \le \frac{\Delta z_{actuator}}{2} \tag{2.19}$$

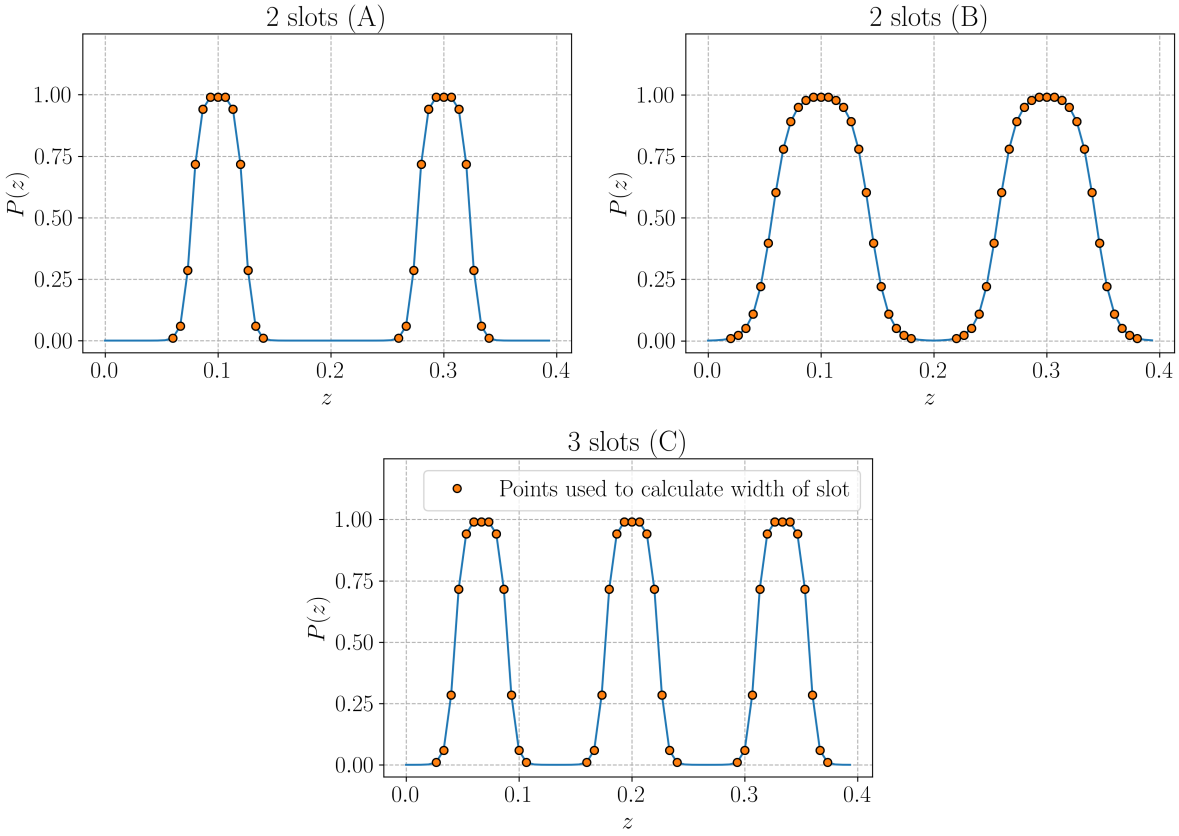

Figure 2.2: Profiles of function $P(z)$ that specifies the spanwise arrangement of actuation.

with their mirrored values. The profiles are then appended until the whole span is covered as can be seen in Fig. 2.2. All investigated actuator arrangements are displayed in Fig. 2.3.

In total, four configurations are tested being two consisting of two slots, one with three slots and one two-dimensional actuator. The configurations with two slots have either narrow (A) or wide (B) spanwise jets. The same narrow jets from configuration (A) are tested in the setup with three slots along the airfoil span. Further details about the 3D actuators used in this work are summarized in Table 2.1.

Table 2.1: Parameters of the 3D actuators from Eq. (2.19). Coefficients α and β are numerical parameters which control the smoothness and stretching of $P_{actuator}(z)$.

	2 slots (A)	**2 slots (B)**	**3 slots (C)**
$\Delta z_{actuator}$	$\approx 0.08L$	$\approx 0.16L$	$\approx 0.08L$
α	-10.62	-3.58	-6.01
β	2.31	2.31	2.31

Simulations with actuation frequencies of $St \in [0.5, 25]$ are first performed for the 2D

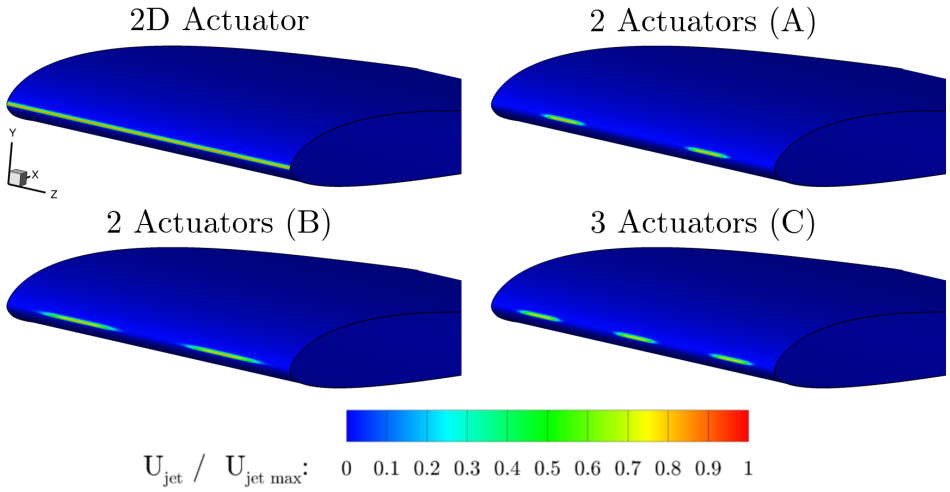

Figure 2.3: Contours showing where U_{jet} is imposed for different actuator arrangements.

actuator with the objective of understanding flow response with respect to this parameter. In order to quantify jet actuation efforts, the coefficient of momentum is calculated according to

$$C_\mu = \frac{\frac{1}{T_g}\int_0^{T_g}\int_{s_0}^{s_n}\int_0^{z_{span}} \rho_\infty U_{jet}(s,z,t)^2 \, ds\, dz\, dt}{0.5\,\rho_\infty U_\infty^2 L\, z_{span}} \,, \tag{2.20}$$

where T_g is the period of $G(t)$. Different values of C_μ are tested to assess the effectiveness of flow control. Table 2.2 displays all configurations investigated in terms of C_μ for all actuator setups. For clarity, we will refer to simulations with a specific C_μ as "Case 1,2 or 3". In what follows, results are obtained for Case 2 at $St = 5$, unless otherwise stated.

Table 2.2: Parameters of control setups investigated. Simulations with the same C_μ are grouped under the same Case category.

Case	C_μ	$\frac{U_{jet\,max}}{U_\infty}$			
		2D Act.	**2 slots (A)**	**2 slots (B)**	**3 slots (C)**
1	1.78e−01%	0.8	-	-	-
2	4.46e−02%	0.4	0.90	0.67	0.74
3	1.12e−02%	0.2	-	-	-

3 Non-actuated Flow

3.1 Flow Configuration and Mesh Convergence Study

Large eddy simulations are performed for a SD7003 airfoil in a plunging motion described by Eq. (2.6) at Reynolds number Re = 60,000, freestream Mach number M = 0.1 and static angle of attack α_0 = 8°. The plunging motion has a reduced frequency k = 0.5 and the plunge amplitude is set as h_o = 0.5L. This specific flow condition was selected based on the availability of results from similar high fidelity simulations from Visbal (2011). In this reference, simulations were performed for different spanwidths. It was concluded that the main flow features were fairly insensitive to spanwidth variations due to the energetic forcing of the plunging motion. Therefore, a span length z_{span} = 0.4L is employed in our calculations similarly to the baseline case from Visbal (2011).

A mesh convergence study is conducted to assess influence of grid resolution on the simulated flows. Figure 3.1 shows detail views of the two grids which are generated with approximately 70% of the surface points located along the suction side of the airfoil. This setup is employed since turbulence appears in this region at various stages of the plunging motion and, hence, finer scales need to be resolved. At the pressure side, however, the flow does not become turbulent at any moment during the plunging motion. The trailing edge of the SD7003 airfoil is rounded in current simulations with an arc of radius r/L = 0.0008. This procedure is required for maintaining the metric terms employed in the structured grid smooth.

The grids parameters are listed in Table 3.1. In this study, we employ resolutions similar to those from Visbal (2011). It is important to mention that a similar numerical approach was used by Visbal (2011) and, therefore, the current investigation follows the best practices needed to properly simulate the current flow. From grid 1 to 2, we mainly improved the spanwise resolution and the concentration of points in the wall-normal direction in the region comprised by a chord length to the airfoil surface. This latter refinement was achieved by changing the stretching function that defines the grid generation.

Simulations of five cycles of plunging motion are performed, but only the last four are

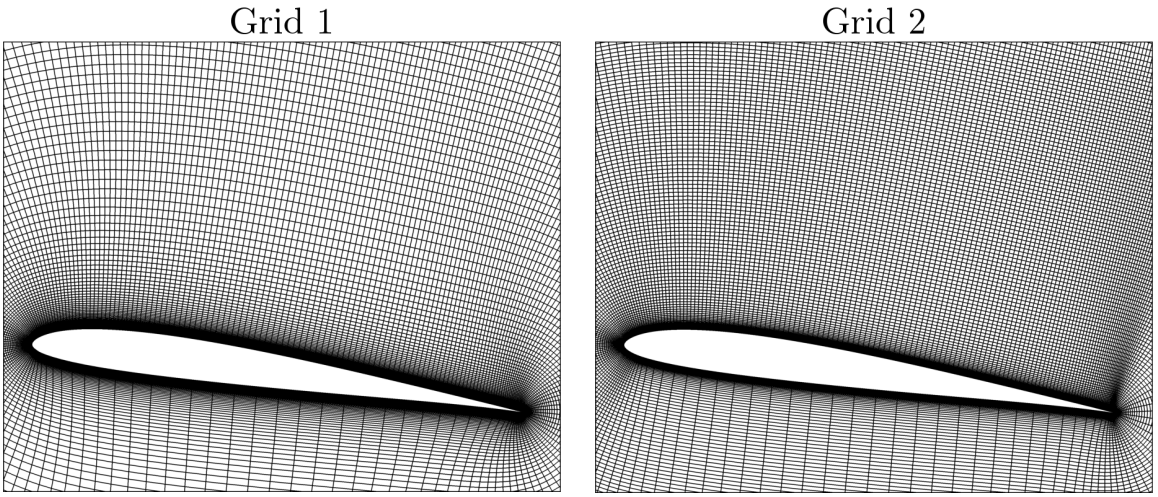

Figure 3.1: Grids considered in the mesh refinement study (only every other grid point in the x-y plane is shown here).

Table 3.1: Grids Parameters.

Grid	ξ^1	ξ^2	ξ^3	$\Delta\xi^2{}_{wall}$	$\Delta\xi^{2^*}$
1	441	300	60	0.00005	0.01
2	481	350	96	0.00005	0.005

$\Delta\xi^2{}_{wall}$: distance between airfoil surface and first grid point in the normal direction
$\Delta\xi^{2^*}$: distance between points in the normal direction one chord away from the airfoil

used to calculate the phase-averaged statistics. Figure 3.2 shows the phase-averaged lift, drag and quarter-chord pitching moment coefficients, C_L, C_D and C_M, respectively, with respect to the effective angle of attack $\alpha = \alpha_0 + \tan^{-1}\left(\frac{kh_0}{L}\cos(kt)\right)$. Results obtained using both grids exhibit good agreement with Visbal (2011), especially considering the variations that occur from cycle to cycle. Such variations can be seen in Fig. 3.3, in which aerodynamic coefficients obtained by the first cycle are already discarded and only the last four are employed in computations. From current results, we consider that the coarser mesh shown in Fig. 3.1 has sufficient resolution to capture the flow physics. Hence, this mesh is chosen to perform the simulations presented in this work. For each cycle, 23,040 computational hours are needed when using the SDUMONT-LNCC cluster.

3.2 Flow Features of Baseline Configuration

This section presents results of the current ILES for the baseline uncontrolled configuration, in which the main physical mechanisms associated with the dynamic stall vortex are described. The current plunge motion undergoes an effective angle of attack in

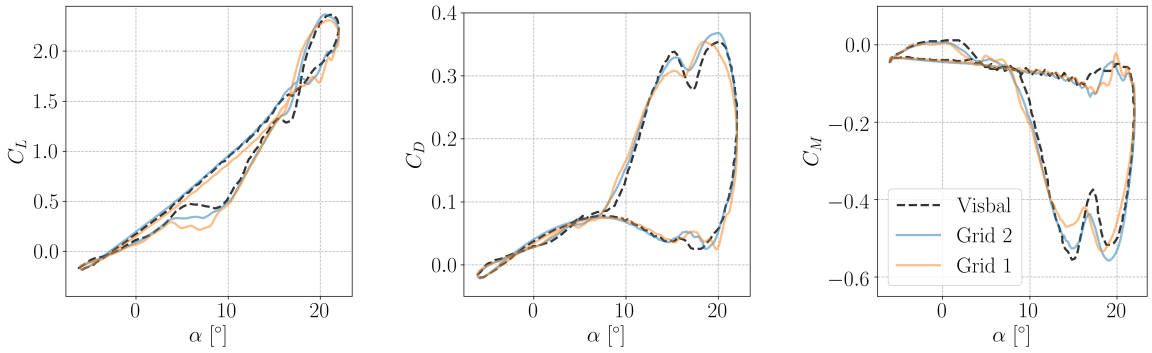

Figure 3.2: Aerodynamic coefficients obtained using grids 1 and 2 and from Visbal (2011) as function of the effective angle of attack α.

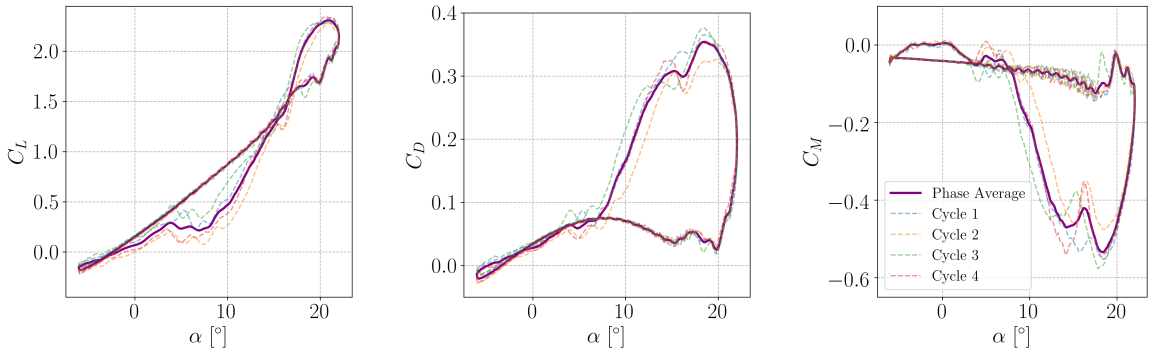

Figure 3.3: Cycle to cycle variations in aerodynamic coefficients (grid 1).

the range of $-6° \leq \alpha \leq 22°$. Due to transients originated from the start of the simulations, only the last four plunging cycles from all five available are used to calculate statistics. For visualization purposes, a phase angle ϕ is used to describe the airfoil position. A schematic of the airfoil motion is shown in Fig. 3.4. At $\phi = 0°$, the airfoil has no vertical velocity and is at the top-most position of the plunging motion. At $\phi = 90°$, it has the highest downward velocity in the y-direction and, at $\phi = 180°$, it has zero vertical velocity being at the bottom-most position of the plunging motion. Finally, at $\phi = 270°$ it has the highest velocity in the y-direction (upward).

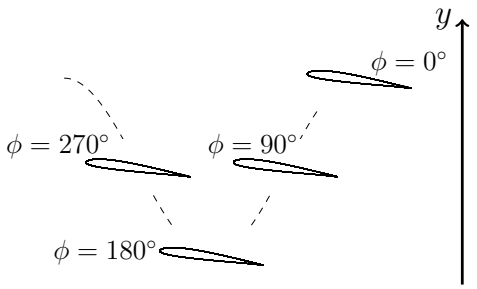

Figure 3.4: Airfoil position for different phase angles ϕ.

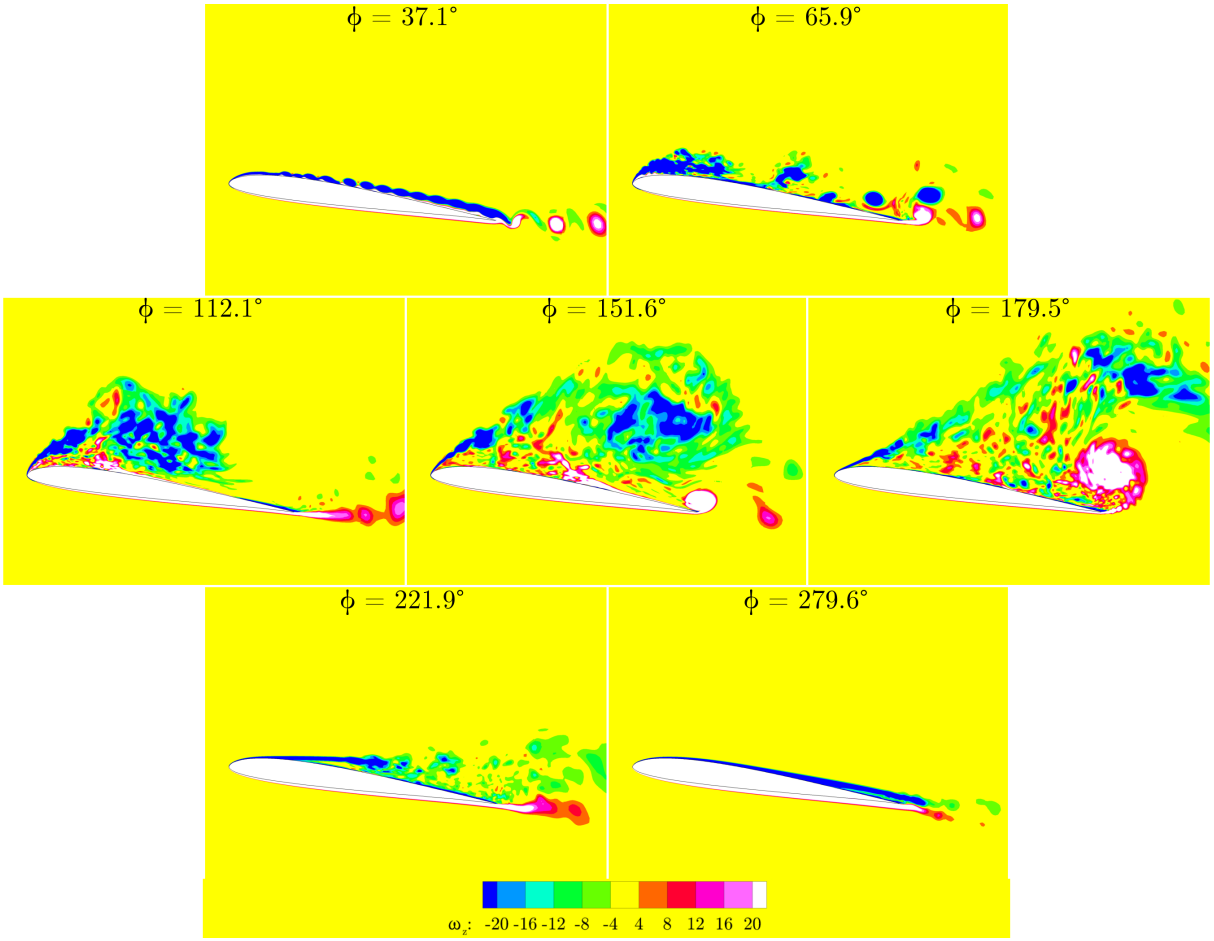

Figure 3.5: Spanwise-averaged z-vorticity contours at different phases of the plunging motion without actuation (see also the Supplemental Material (Ramos, 2019e)).

Fig. 3.5 and Supplemental Material (Ramos, 2019e) presents spanwise-averaged z-vorticity contours at different phases of the plunging cycle. During the downstroke, flow instabilities begin to grow in the shear layer formed along the suction side of the airfoil with vortex shedding occurring at the airfoil wake when ϕ = 37.1°. As the downward motion continues, instabilities on the suction side grow and eventually break the large spanwise-correlated structures into finer ones, leading to a transitional flow. While this takes place, the main leading-edge vortex (LEV) begins to form (ϕ = 65.9°). The LEV grows over the suction side (ϕ = 112.1°), increasing lift and creating a nose-down pitching moment.

As the LEV covers the entirety of the chord, a trailing-edge vortex (TEV) forms and "lifts" the LEV away from the airfoil surface at ϕ = 151.6°. As the LEV lifts off, an oscillation in the pitching moment can be observed. As the airfoil motion continues, the TEV is ejected from the suction side (ϕ = 179.5°). When the airfoil moves upwards, re-laminarization starts from the leading edge (ϕ = 221.9°) and keeps going until the entire boundary layer is relaminarized (ϕ = 279.6°). Subsequently, the Kelvin–Helmholtz

instability can be observed again, leading to periodic shedding of vortices from the trailing edge.

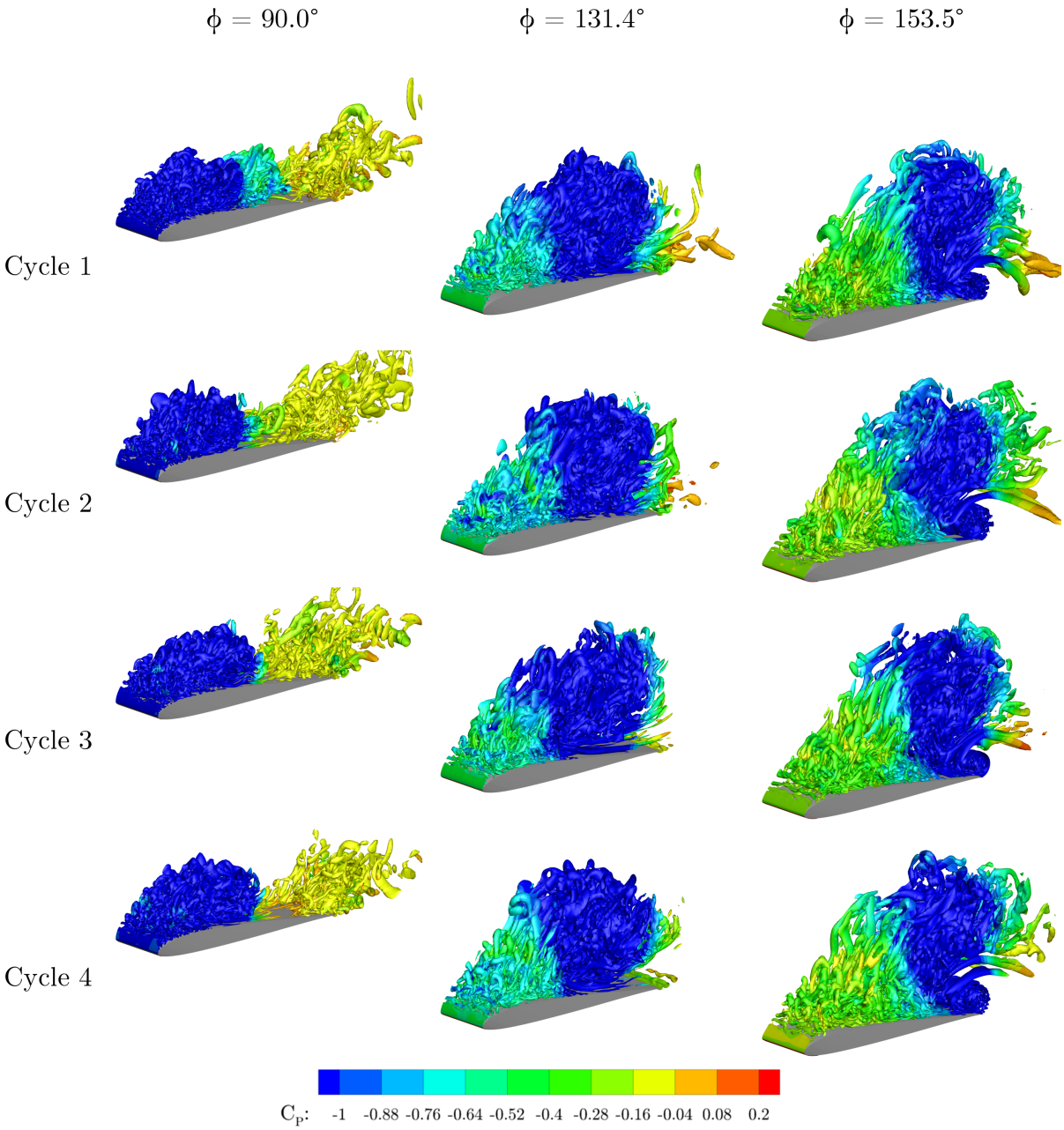

Figure 3.6: Iso-surfaces of Q criterion colored by C_P at different phases of the plunge motion without actuation.

In order to further characterize the current flow, iso-surfaces of Q-criterion are shown in Fig. 3.6 for all cycles. The turbulent structures are colored by pressure coefficient contours. Despite subtle cycle to cycle variations, the main features of the dynamic stall process remain unchanged. Namely, the formation of the LEV, its transport over the airfoil, the formation of the TEV and the departure of both vortices. Although fine turbulent structures can be observed, it is clear that large-scale coherent structures are

the most prominent in the dynamic stall process. We expect such energetic structures to play a key role in the dynamics of the present flow, severely impacting the aerodynamic loads. For example, the leading-edge vortex is characterized by a low pressure region which is advected along the suction side, dynamically affecting flight stability through changes in lift and drag forces during the plunging motion.

Simulations of a static SD7003 airfoil were also conducted using the present numerical methodology to expose the different flow features for the same effective angles of attack. Figure 3.7 shows the aerodynamic coefficients obtained for the airfoil under downstroke motion and simulations of the static airfoil at different angles of attack. The orange lines represent the aerodynamic coefficients computed only during downstroke while the corresponding values computed for the static case are depicted by vertical bars. These bars indicate the amplitude variations of lift, drag and pitching moment coefficient experienced for the static case. The ranges of minimum and maximum values of all aerodynamic coefficients for the static airfoil cases are clearly different when compared to those obtained for dynamic stall, with exception of C_M at $\alpha = 22°$. When looking only at the simulations with the static airfoil, it can be seen that the differences between maximum and minimum values, indicated by vertical bars, grow as α increases due to intensification of vortex shedding in a stalled condition. From this figure, one can see that drag continuously increases with the angle of attack. Mean lift decreases from $\alpha = 8°$ to $15°$ as expected for static stall. However, it increases again as the incidence changes to $\alpha = 22°$, probably because of the intense pressure fluctuations observed for this configuration.

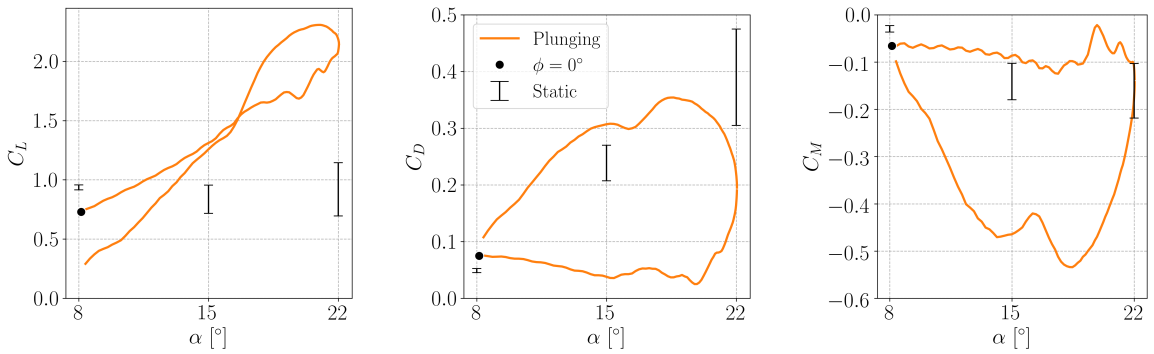

Figure 3.7: Aerodynamic coefficients of phase averaged data from simulation of plunging airfoil versus effective angles of attack. From left to right, the angles of attack are $\alpha = 8°$, $15°$ and $22°$, respectively. Bars representing maximum and minimum values found in simulations of a static airfoil.

The differences among simulations with and without motion becomes even clearer in Fig. 3.8. It is important to notice that since the airfoil has downstroke and upstroke motions and, hence, all angles of attack in the range $-6° < \alpha < 22°$ occur for two separate moments. The contours appearing in the middle column are those which happen first

in the plunging motion, when starting from $\phi = 0°$. For the static case at $\alpha = 8°$, the flow is turbulent and attached, while during downstroke in the plunging motion (middle column) there is no sign of three-dimensional effects on the airfoil suction side. On the other hand, during upstroke, when this effective angle of attack is reached, the flow exhibits three-dimensional structures ejecting from the suction side besides a large coherent structure which is shed.

At $\alpha = 15°$, static stall has taken place and a considerable recirculation region can be identified in blue colors in Fig. 3.8. On the other hand, during downstroke, Kelvin-Helmholtz instabilities arise originated from the shear layer for the first time at $\alpha = 15°$. During the upstroke, turbulent structures are present and the flow is massively separated because of the dynamic stall vortex. At $\alpha = 22°$, the static airfoil has far exceeded the stall sngle and the flow is completely separated. Intense vortex shedding is present, which explains the high variance of aerodynamic coefficients observed in Fig. 3.7. When the airfoil is moving, it reaches this angle of attack in the middle of the downstroke motion. At this moment, the dynamic stall vortex is being formed and vorticity starts to accumulate near the leading edge, forming an attached flow region in the mid-chord region of the airfoil and a mildly separated region at the trailing edge.

It is clear that, for the plunging airfoil, the emergence of the dynamic stall vortex changes the flow quite drastically when compared to its static stall counterpart. Next section describes the efforts towards controlling the formation of this large-scale structure aiming to reduce the overall drag and its fluctuations, while trying to maintain mean lift unaltered.

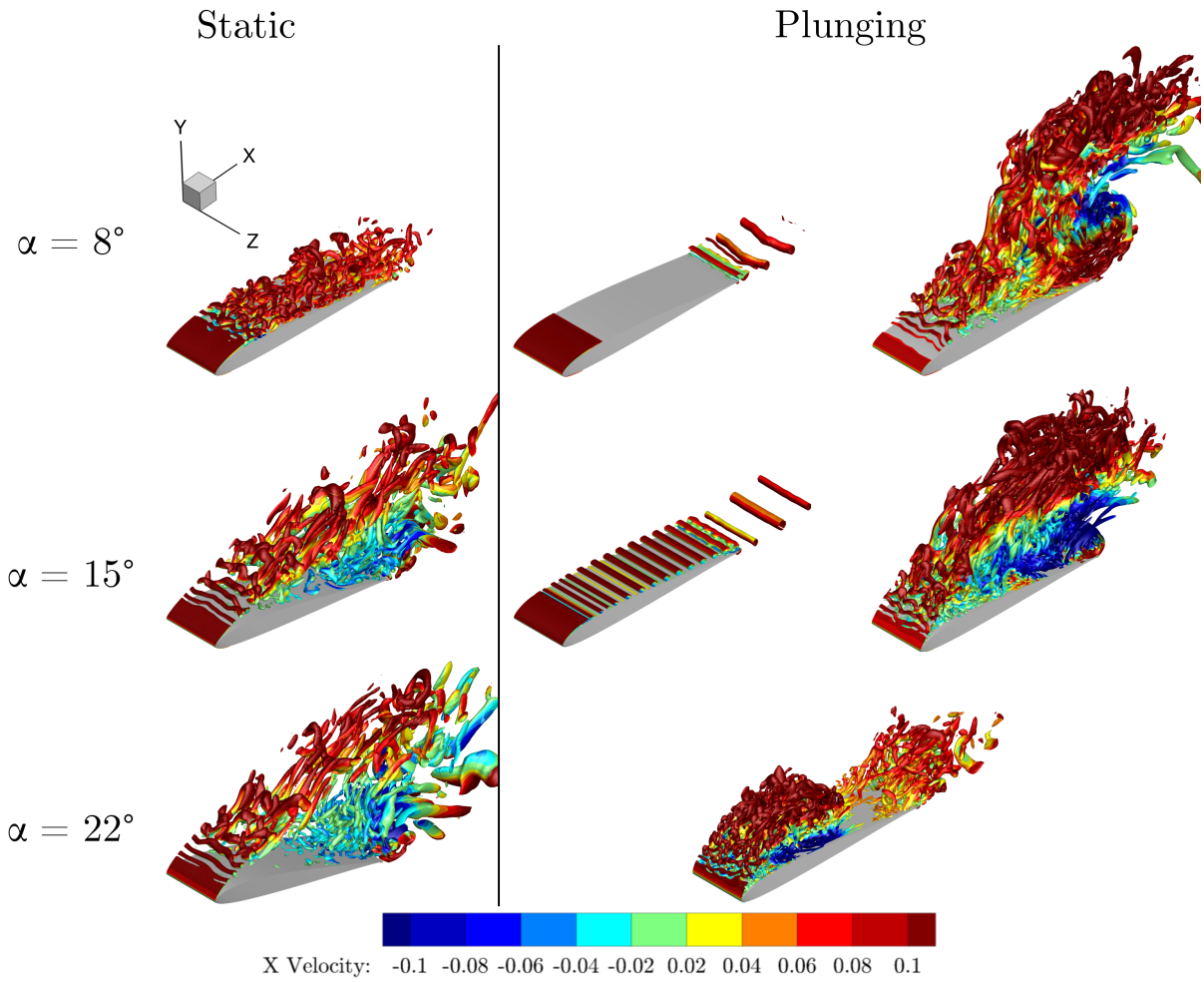

Figure 3.8: Q-criterion colored by X Velocity for different flows undergoing static stall and the plunging airfoil at similar effective angles of attack.

4 Active Flow Control

4.1 2D Actuation

An assessment of 2D actuation on the flow dynamics performed only in one cycle is presented in this section. Flow actuation is turned on at ϕ = 0° after five plunging cycles. Figure 4.1 shows the averaged values of C_L, C_D and C_M represented by black dots for different actuation frequencies St. The maximum and minimum values of the aerodynamic coefficients computed during the cycle are given by the top and bottom values of each bar. Results obtained for the baseline configuration are depicted by orange bars while green, blue and red bars represent solutions computed for cases 1, 2 and 3, respectively, as described in Table 2.2. It is important to remind that the coefficient of momentum C_μ for case 1 is the highest investigated while that for case 3 is the lowest. Hence, this figure allows an assessment of the effects of 2D actuation in terms of both actuation frequency and its intensity on the aerodynamic coefficients.

From Fig. 4.1, it can be noticed that C_L do not exhibit large variations for the actuation frequencies and C_μ considered. However, significant changes in C_D and C_M are observed depending on the actuation frequency. For example, large reductions in C_D appear in the range $2.5 < St < 15$ compared to the baseline case for all values of C_μ investigated. Frequencies higher than St = 15 or lower than St = 2.5 do not promote a significant impact on drag and pitching moment, both in terms of mean values and maximum and minimum amplitudes. The coefficient of momentum also has a significant impact on the results. In general, for the flows with stronger actuation disturbances (cases 1 and 2), reductions in maximum drag are more evident. In some occasions, better results in terms of drag reduction are observed for Case 2.

Averaged values of C_L and C_D normalized by their respective baseline values are displayed in Fig. 4.2. This figure also shows a drag polar plot relating $\frac{\overline{C_L}}{\overline{C_D}}$. Again, results are presented as a function of Strouhal number and coefficient of momentum. The behavior observed for the maximum and minimum values of aerodynamic coefficients is similar to their averaged values. For example, with St = 3.75 and C_μ from case 1, the airfoil drag coefficient C_D is reduced to 30% of the baseline. For the same case, the lift coefficient C_L only drops to 86% of the baseline. In summary, for cases 1 and 2 and Strouhal numbers in the range $2.5 \leq St \leq 15$, flow actuation is able to considerably reduce

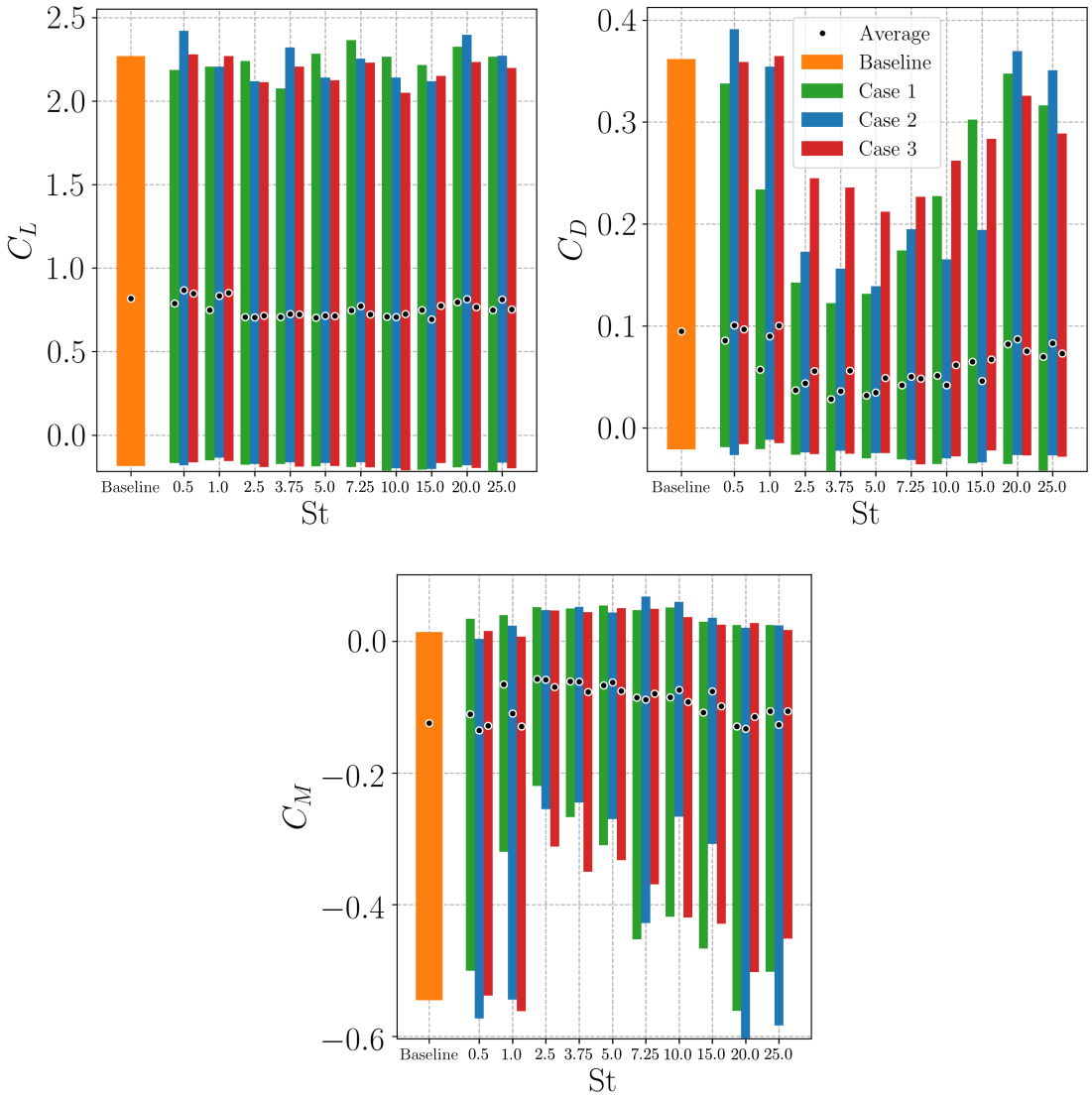

Figure 4.1: Variations in aerodynamic coefficients for different actuation frequencies (St) and coefficient of momentum (C_μ) for 2D actuated flows. We refer to simulations with different C_μ as "Case 1,2 or 3".

mean values of drag coefficient without severely impacting lift. From the figure, one can conclude that the best results in terms of mean lift to mean drag ratio are obtained for frequencies given by St = 3.75 and 5.0.

Figure 4.2 also shows the impact of actuation in the aerodynamic damping Ξ, which is calculated as

$$\Xi = -\frac{1}{\alpha_{max} - \alpha_0} \oint C_M \mathrm{d}\alpha \ . \tag{4.1}$$

It can be seen that the baseline flow has negative damping, implying that energy is transferred from the flow to the airfoil, leading to oscillations and even flutter. While some actuation frequencies, e.g. cases 2 and 3 at St = 0.5, lead to even more negative values of aerodynamic damping, frequencies around St = 3.75 successfully revert the issue,

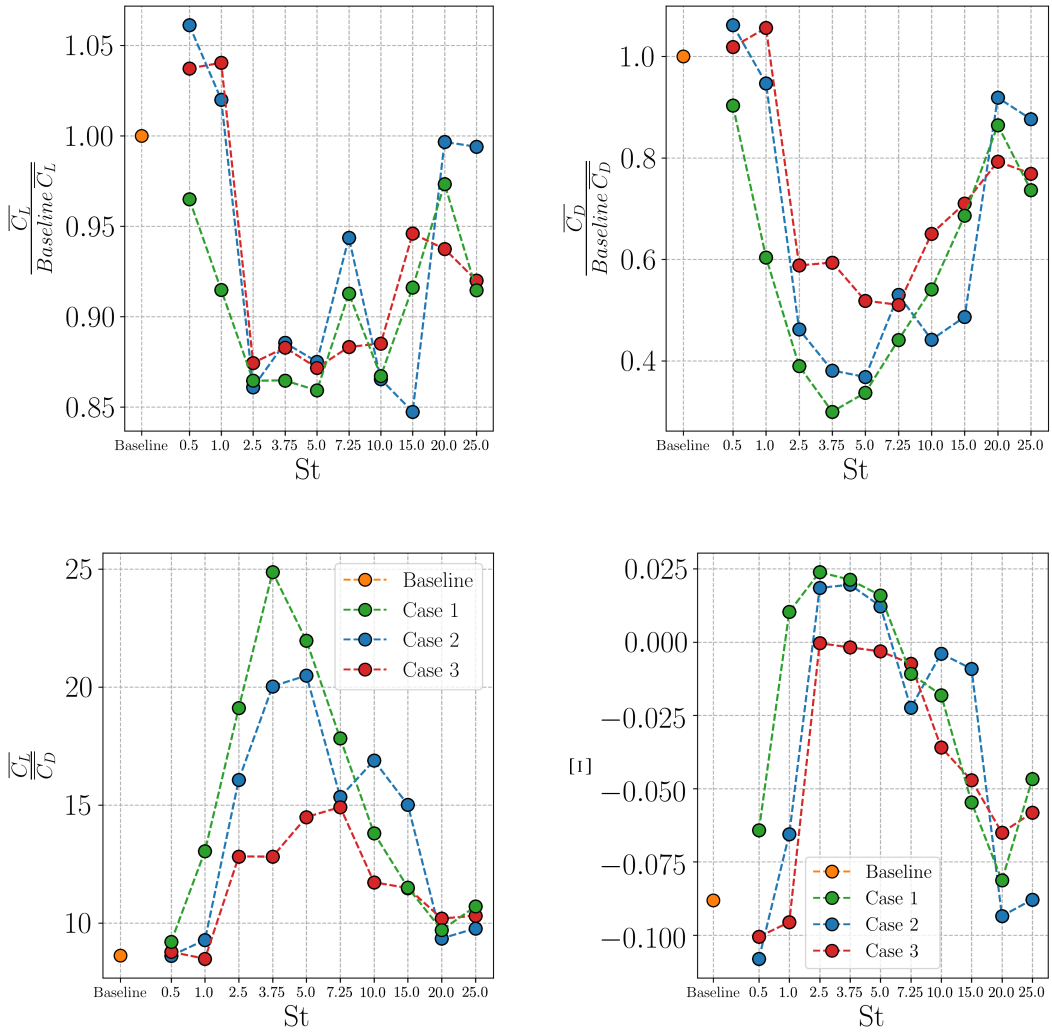

Figure 4.2: Mean aerodynamic loads compared to the baseline flow, mean lift to mean drag ratio, and aerodynamic damping using 2D actuation.

leading to a positive damping and a stabilizing effect on the airfoil dynamics.

In what follows, results will be discussed based only on "Case 2" flow actuation. Figure 4.3 shows plots of aerodynamic coefficients as functions of the effective angle of attack. Results of the baseline flow are compared to those with actuation for St = 1, 5 and 25. Hence, it is possible to evaluate the effects of low, moderate and high frequencies of actuation on the aerodynamic loads during any instant of the motion. It is clear that the actuation frequency has a large impact in the flow response, especially for instants of downward velocity.

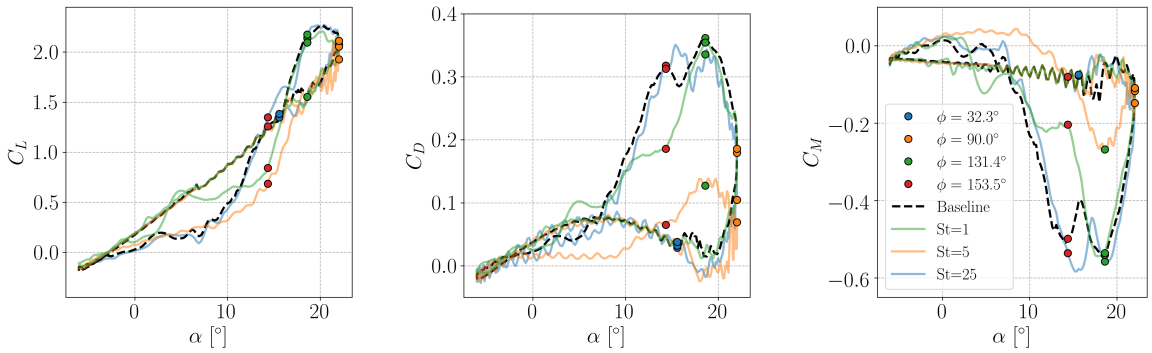

Figure 4.3: Aerodynamic coefficients versus effective angle of attack for 2D actuated flows with different frequencies (Case 2).

Different moments of the plunging motion are also highlighted by circles at $\phi = 32.3°$, 90.0°, 131.4° and 153.5°. One should be reminded from Fig. 3.4 that $\phi \in [0°, 180°]$ represents the downstroke motion which includes the formation, transport and ejection of the leading-edge vortex. These specific values of ϕ are shown due to important flow features that occur at such instants and that will be used to compare the actuation setups next.

Contours of spanwise-averaged pressure coefficient C_P with iso-contours of z-vorticity are shown in Fig. 4.4 and the Supplemental Material (Ramos, 2019a) for the same actuation frequencies as in Fig. 4.3 and for the baseline case. It is observed that actuation does not delay the formation of the dynamic stall vortex but disrupts it. At $\phi = 32.3°$, all flows have roughly the same aerodynamic loads (notice that the blue circles lie on top of each other in Fig. 4.3). However, the shear layer is clearly disrupted by actuation, especially in the $St = 5$ case. When compared to the baseline case, it can be seen that Kelvin-Helmholtz instabilities appear and grow earlier in the plunging motion for the $St = 5$ setup. Actuation at other frequencies also modify the shear-layer but instabilities do not get amplified as much. At $\phi = 90.0°$ (maximum downward velocity), the formation of the leading-edge vortex does not occur as prominently in the $St = 5$ case when compared to other actuation frequencies. For this case, vortices created by actuation successfully

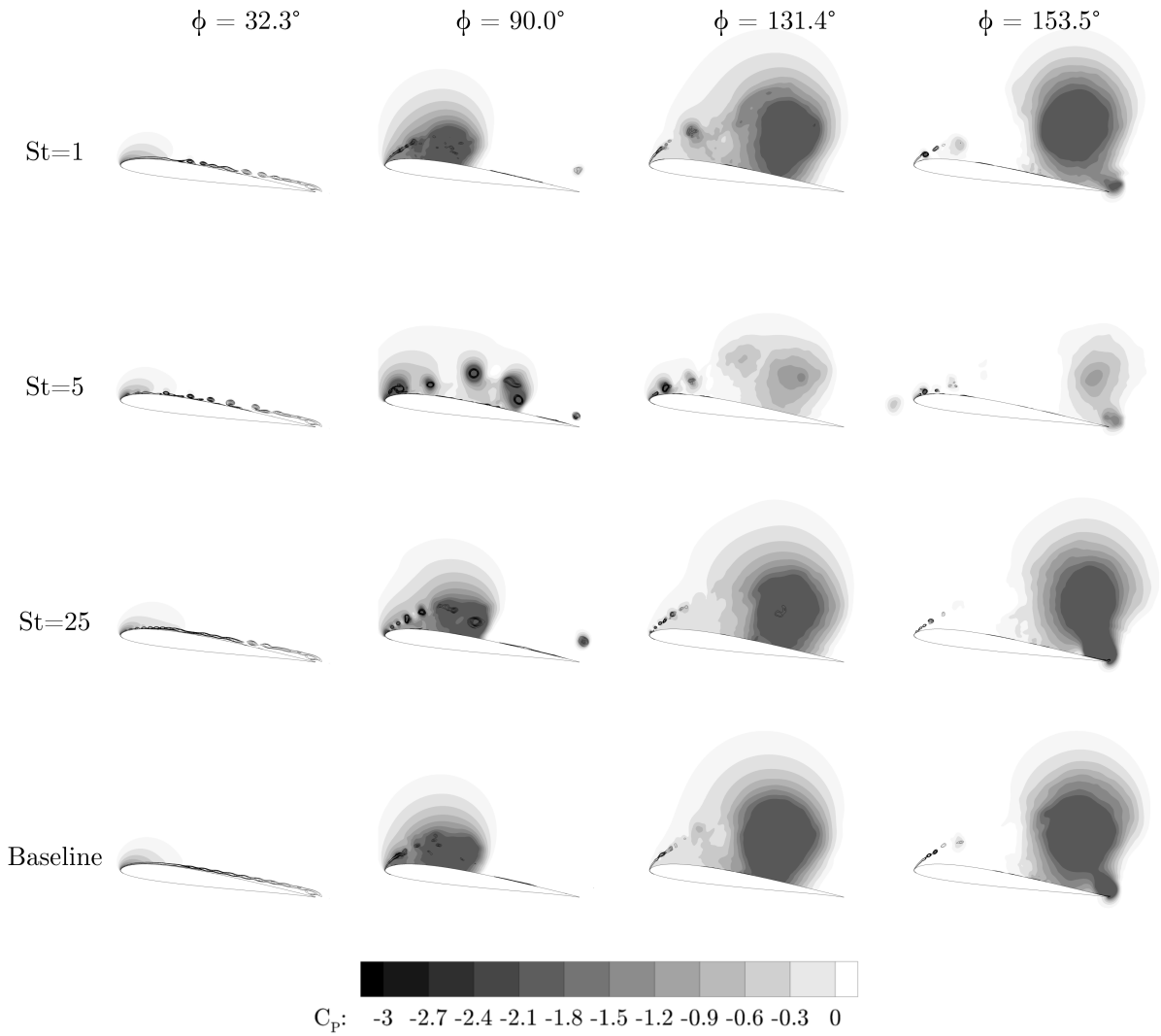

Figure 4.4: C_P contours with iso-lines of z-vorticity for spanwise-averaged flows with 2D actuation (Case 2).

break the large-scale coherent structure formed at the leading edge. On the other hand, for St = 1 and 25, the vortices created by the actuation do not effectively disrupt the formation of the LEV. In the latter case, small vortical structures end up coalescing and forming the LEV in a similar fashion compared to the baseline flow.

At ϕ = 131.4° we observe in Fig. 4.3 the highest value of C_D for the baseline flow. Actuated flows exhibit similar aerodynamic coefficients, except for St = 5. At this frequency, Fig. 4.4 shows a coherent structure with higher (less negative) values of C_P compared to other cases. This effect is a consequence of the formation of smaller vortical structures by the actuation that do not coalesce into a single dynamic stall vortex at first. This weaker LEV also induces the formation of a less intense TEV at ϕ = 153.5°. This latter instant is represented in Fig. 4.3 by a second peak in drag coefficient for the baseline flow. It is worth noting that the amount of energy used by the actuators is very

small. For example, when the actuation frequency $St = 5$ is considered, the energy used by the actuator is only 0.015% of the total amount of saved energy due to drag reduction.

Figure 4.5 shows C_P distributions (spanwise-averaged) in order to better quantify pressure differences among the various flows previously analyzed. Results are presented at $\phi = 131.4°$ and 153.5° as a function of the airfoil chord location. A vertical dashed line marks the position where the surface normal on the airfoil wall (on the suction side) is vertical, as shown in Fig. 4.6. This position is given by $x_{vsn} = 0.12L$ and it is important to differentiate how the regions over the airfoil suction side contribute to drag reduction. We consider the surface normal pointing inward the airfoil. Lift and drag generated from pressure distributions along the airfoil surface are calculated by $L = \oint p\, n_y\, dS$ and $D = \oint p\, n_x\, dS$, respectively. Here n_x is the component of surface normal in the x direction while n_y is that in the y direction. Thus, a force applied in the normal direction on the airfoil suction side, to the left of the vertical dashed line, leads to lift reduction and drag increase. On the other hand, a normal force applied to the right of such line result in both lift and drag reductions. Pressure forces applied on the bottom side of the airfoil will always lead to lift increase.

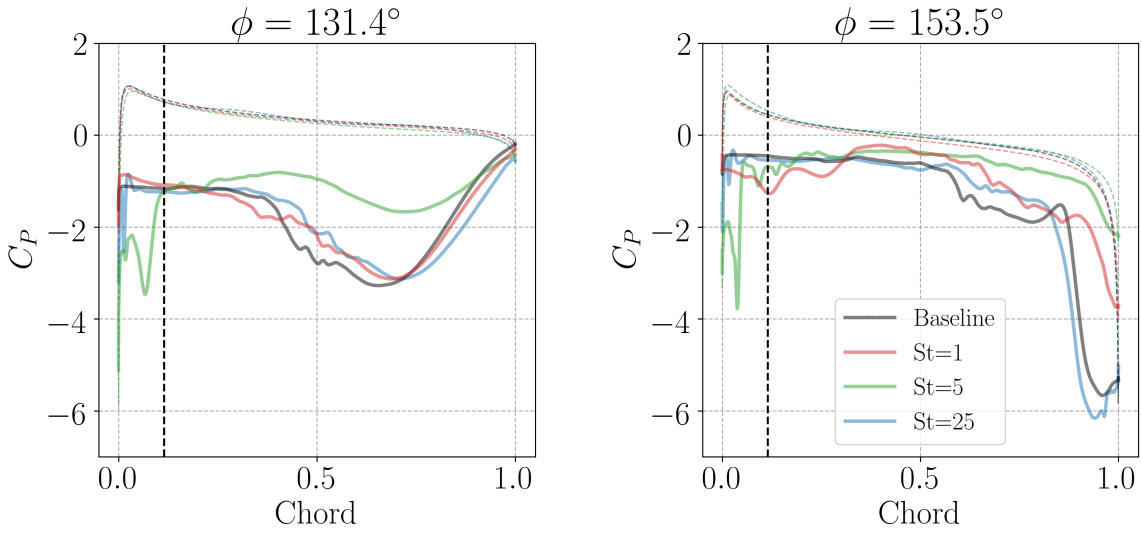

Figure 4.5: Comparison between span-averaged values of C_P for 2D actuators with different frequencies (Case 2). The vertical dashed line indicates the location of x_{vsn}.

For the baseline case, at $\phi = 131.4°$, the bump in the C_P distribution appears due to the advection of the LEV over the suction side of the airfoil. This negative value of pressure coefficient indicates that a strong suction occurs on the top surface of the airfoil, leading to a lift and drag increase. Similar trends are observed for the cases with $St = 1$ and 25. At $\phi = 153.5°$, a strong suction peak is observed at the trailing edge due to the formation of the TEV and such feature also increases both lift and drag. Again, the

solution obtained for $St = 25$ is very similar to that from the baseline flow. On the other hand, for the $St = 5$ setup, one observes that a mild bump forms at $\phi = 131.4°$, reducing both lift and drag for this case. However, a strong suction peak is present at the leading edge of the airfoil, increasing both lift and further reducing drag. When the airfoil is at $\phi = 153.5°$, a suction peak is still present at the airfoil leading edge and a minor suction effect is observed at the trailing edge due to a less intense TEV. In summary, lower (more negative) values of C_P to the left of the vertical dashed line in Fig. 4.5 would result in lower pressure drag. In the same context, higher (less negative) values of C_P to the right of the vertical dashed line also lead to lower pressure drag. Both conditions are met when flow actuation is applied at $St = 5$.

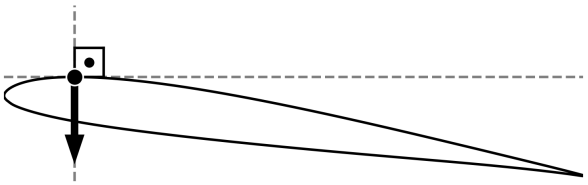

Figure 4.6: Position x_{vsn} where the inward pointing surface normal at the suction side is vertical.

The full history of spanwise-averaged C_P computed on the airfoil suction side is displayed in Fig. 4.7 as a function of ϕ. In this figure, a comparison is shown for the baseline and $St = 5$ cases. The dark blue colors in the plots represent the low pressure signatures from the LEV and TEV and one can see that they are less severe in the case with control. Figure 4.8 shows similar maps but colored by friction coefficient C_f instead. For lower ϕ angles, it is possible to notice the oscillatory behavior of C_f due to the initial shear layer instabilities. The dark blue contours mark the separation region caused by the transport of the LEV while the dark red contours in the trailing edge are due to formation of the TEV. In the case with actuation, the LEV is weaker so the blue trace is thinner and less intense than that computed for the baseline configuration. From this figure, it is also possible to see that the separation near the leading edge has an oscillatory behavior due to flow actuation during the downstroke motion.

The $St = 5$ actuation leads to a disruption of the LEV which sheds small pockets of vorticity instead of accumulating it. This effect can be observed in Fig. 4.9 and it avoids the formation of a large-scale coherent structure at the leading edge, in contrast to the baseline configuration (see also the Supplemental Material (Ramos, 2019e)). In summary, a significant reduction in C_D and C_M occurs as a result of the features observed due to flow actuation: mitigation of the dynamic stall vortex, strong negative values of C_P upstream of x_{vsn}, and mild values of C_P downstream of x_{vsn} for $2.5 < St < 15$. Although

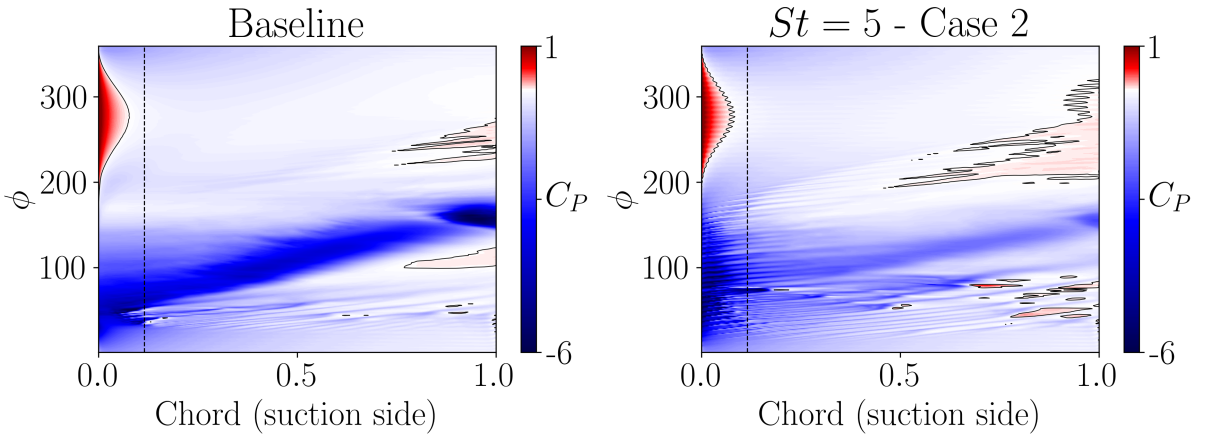

Figure 4.7: Comparison of C_P between baseline and 2D actuated flow with $St = 5$.

the flow actuation leads to a small reduction in terms of C_L, it is not as prominent as the reductions observed in C_D and C_M. Since a lower actuation disturbance is employed for Case 2, and the best result in terms of $\frac{\overline{C_L}}{\overline{C_D}}$ for this case is obtained for $St = 5$, we will further investigate this specific flow configuration. Therefore, we can reduce the energy expenditure in the actuation while maintaining the mean lift to mean drag ratio above 20.

4.2 3D Actuation

In the previous section, results of 2D flow actuation for the present plunging airfoil were presented. However, 3D actuation can enhance performance when it comes to drag reduction of an airfoil in static stall condition, as shown by Yeh and Taira (2019) and Munday and Taira (2018). Therefore, we present a study of different configurations of 3D actuation to assess their impact on drag reduction. Results are shown for $St = 5$ and C_μ

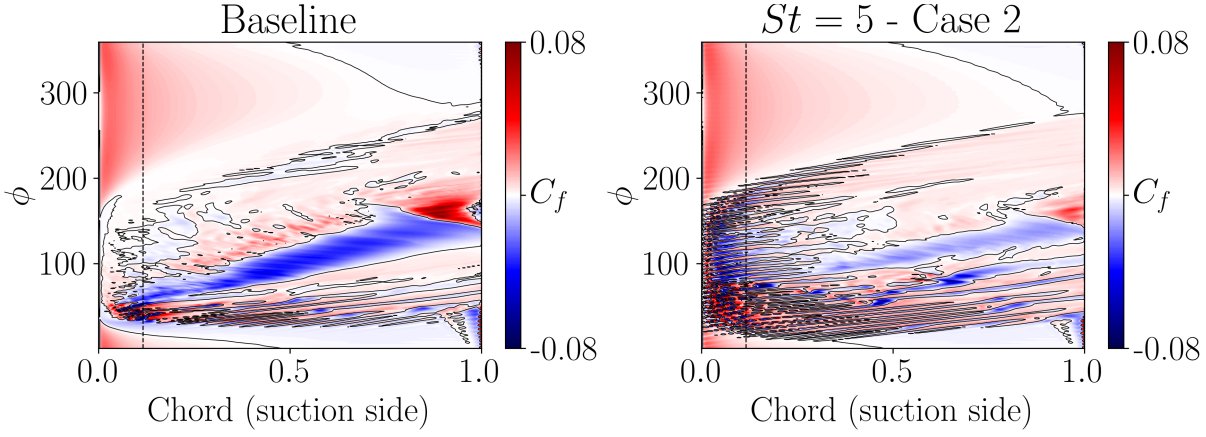

Figure 4.8: Comparison of C_f between baseline and 2D actuated flow with $St = 5$.

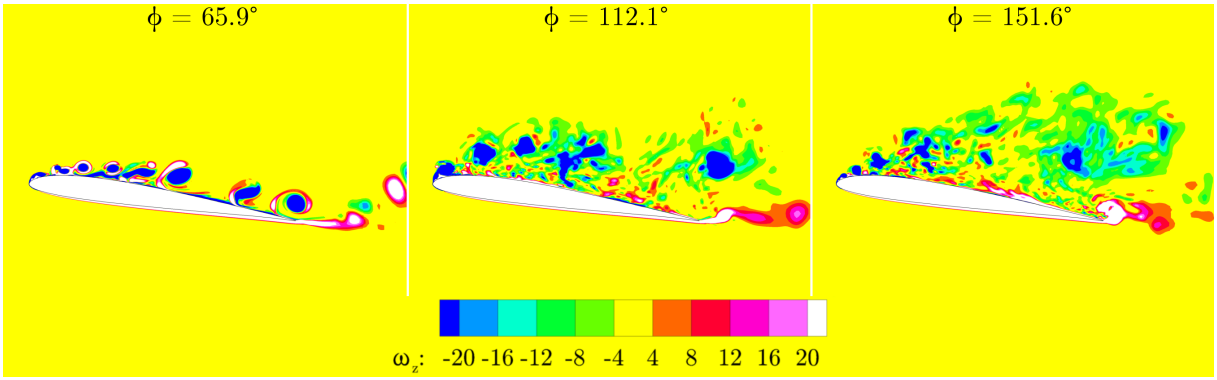

Figure 4.9: Spanwise-averaged z-vorticity contours at different phase angles for the 2D $St = 5$ controlled case with 2D actuation (Case 2).

from Case 2 for the actuation configurations discussed in Section 2.3.

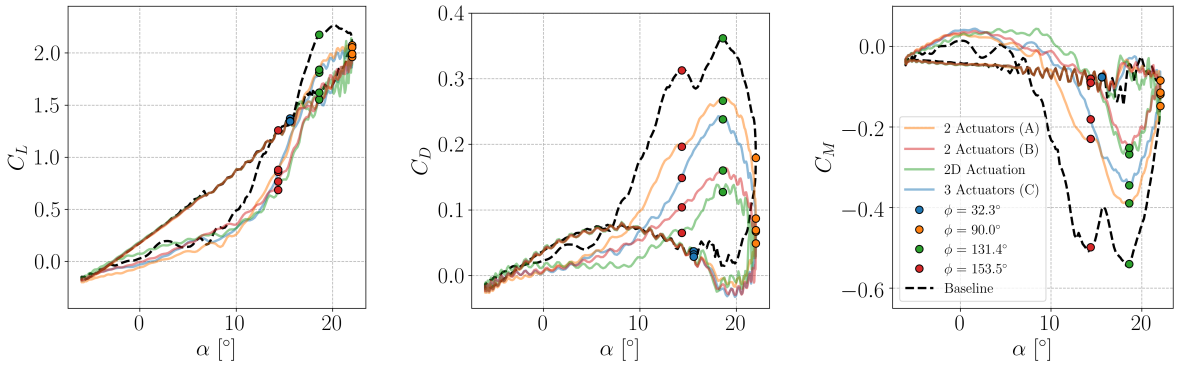

Figure 4.10: Comparison of aerodynamic coefficients obtained by 2D and 3D actuation with $St = 5$ (Case 2).

In Fig. 4.10, results are shown for the aerodynamic coefficients and it can be seen that all cases with 3D actuation exhibit higher values of C_L for high effective angles of attack α when compared to the 2D actuated flow. However, the values of C_D are considerably lower for the 2D actuation at the same angles of attack. The same can be said for C_M, except for the case with two larger slots (configuration B), which has comparable values of moment coefficient to those obtained for the 2D actuation.

Iso-surfaces of Q-criterion colored by pressure coefficient are shown in Fig. 4.11 at various moments of the plunge motion. A movie with the same features is presented as Supplementa Material (Ramos, 2019c). Due to its inherent three-dimensionality, 3D actuation exhibits earlier transitional features at $\phi = 32.3°$ when compared to the baseline and 2D actuation cases. All actuated flows exhibit weaker LEVs compared to the baseline, noting that 2D actuation is the most efficient since it is able to efficiently disrupt the LEV formation at $\phi = 90.0°$. At $\phi = 131.4°$, we can notice that both 2D actuation and that with two wider slots (B) produce dynamic stall vortices with higher values (less negative) of pressure coefficient. With weaker LEVs, these cases also show TEVs which are less

intense, avoiding the secondary drag peak that appears for the baseline configuration in Fig. 4.10 at $\phi = 153.5°$.

The impact of different types of actuation on C_P distribution along the airfoil suction side can be seen in Fig. 4.12 and in the Supplemental Material (Ramos, 2019b). At $\phi = 32.3°$, despite similar values of aerodynamic loads observed in Fig. 4.10, C_P contours are fairly distinct. Two-dimensional coherent structures are present in the baseline and 2D actuation cases, while all 3D actuated flows exhibit more complex 3D structures which promote transition to turbulence earlier in the plunging motion. When C_D reaches its peak at $\phi = 131.4°$, a dark region of low pressure created by the LEV is present in the baseline flow, while milder values of C_P are observed in the actuated cases. In general, the 2D actuated flow has less negative values of C_P downstream of x_{vsn} when compared to the other cases and the C_P values are more negative upstream x_{vsn}. Similar observations can be made at $\phi = 153.5°$ regarding the TEV.

Fig. 4.13 and the Supplemental Material (Ramos, 2019d) shows how the flow separation changes due to actuation. While the flow is fully two-dimensional in the baseline and 2D actuated cases at $\phi = 32.3°$, the same cannot be said for the cases with 3D actuation. After transition takes place, regions of separation and reattachment upstream of x_{vsn} show higher spanwise coherence in the 2D actuated flow. Nevertheless, as can be seen at $\phi = 131.4°$, the separation created by the LEV is attenuated in all control cases. At $\phi = 153.5°$, all the actuated flows are able to form the TEV further downstream compared to the baseline case, reducing its overall impact on the aerodynamic coefficients.

Finally, Fig. 4.14 presents a comparison of spanwise-averaged values of C_P for different configurations of actuation. One can see that the 2D actuation leads to lower values of C_P at the leading edge, increasing lift and reducing drag. At the same time, the suction effects towards the trailing edge are milder for this case, further reducing drag. Values of mean lift to mean drag ratio, as well as aerodynamic damping, are displayed in Table 4.1 for different actuation setups. The best results of $\frac{\overline{C_L}}{\overline{C_D}}$ are found for the 2D actuation followed by that with two wider slots (B). The same trend is observed when analyzing values of aerodynamic damping. In summary, it can be observed that when a larger region on the leading edge is covered by the slots, making it more similar to a 2D configuration, the better the results are in terms of drag reduction and aerodynamic damping increase.

Table 4.1: Mean lift to mean drag ratios and aerodynamic damping for different actuation configurations with $St = 5$ (Case 2).

	2D Act.	**2 Slots (A)**	**2 Slots (B)**	**3 slots (C)**
$\frac{\overline{C_L}}{\overline{C_D}}$	20.48	12.03	19.13	14.73
Ξ	0.0122	-0.0318	0.0066	-0.0146

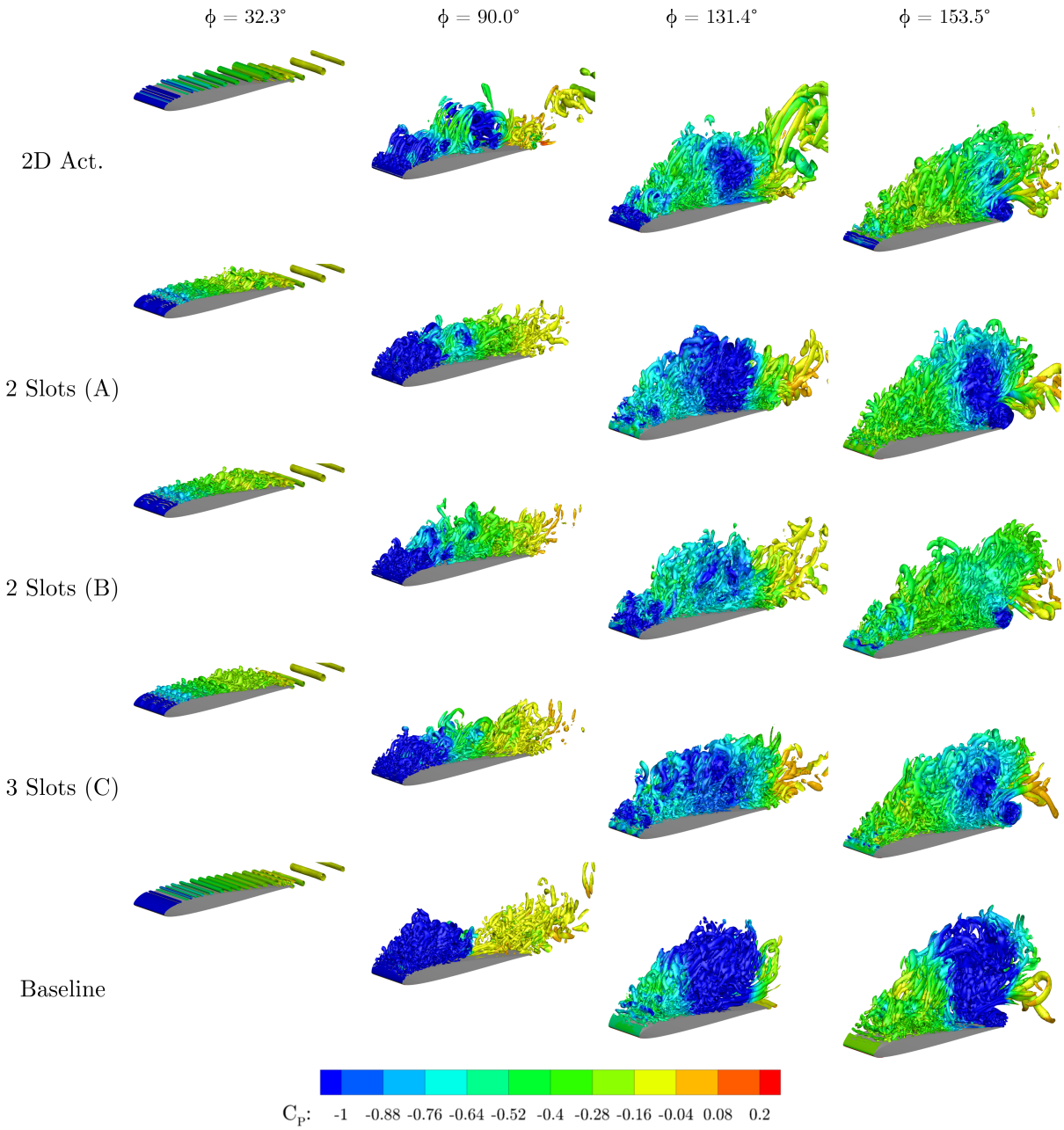

Figure 4.11: Q-criterion colored by C_P comparing 2D and 3D actuation with $St = 5$ (Case 2) at various phases of the plunge motion.

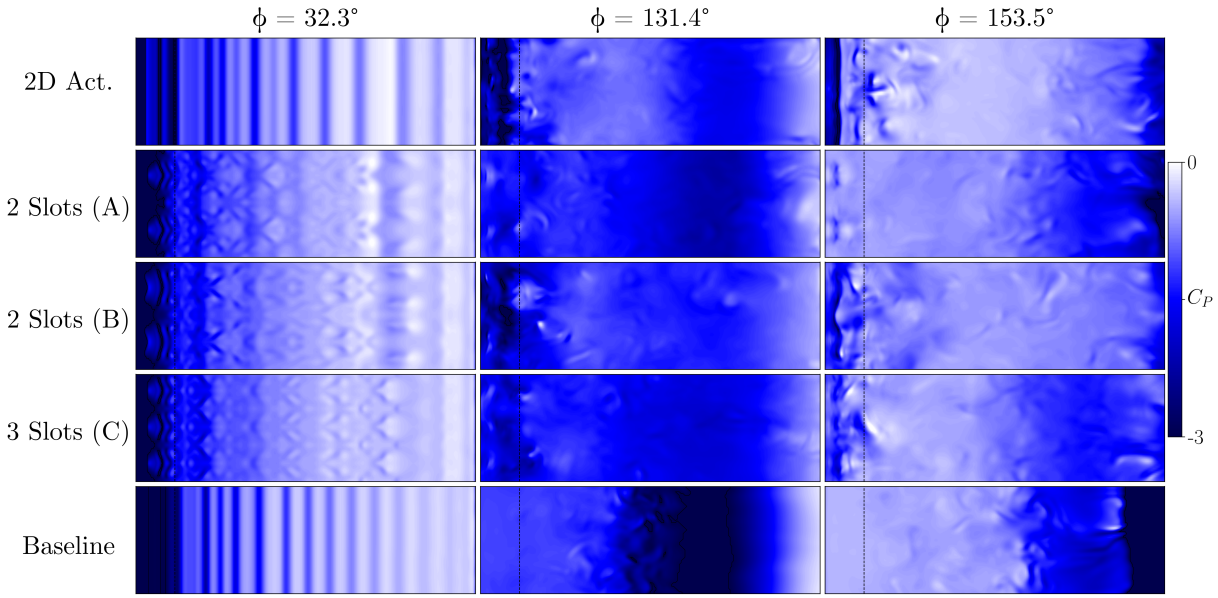

Figure 4.12: Distribution of C_P over the airfoil suction side (flow is directed from left to right) for 2D and 3D actuation with $St = 5$ (Case 2).

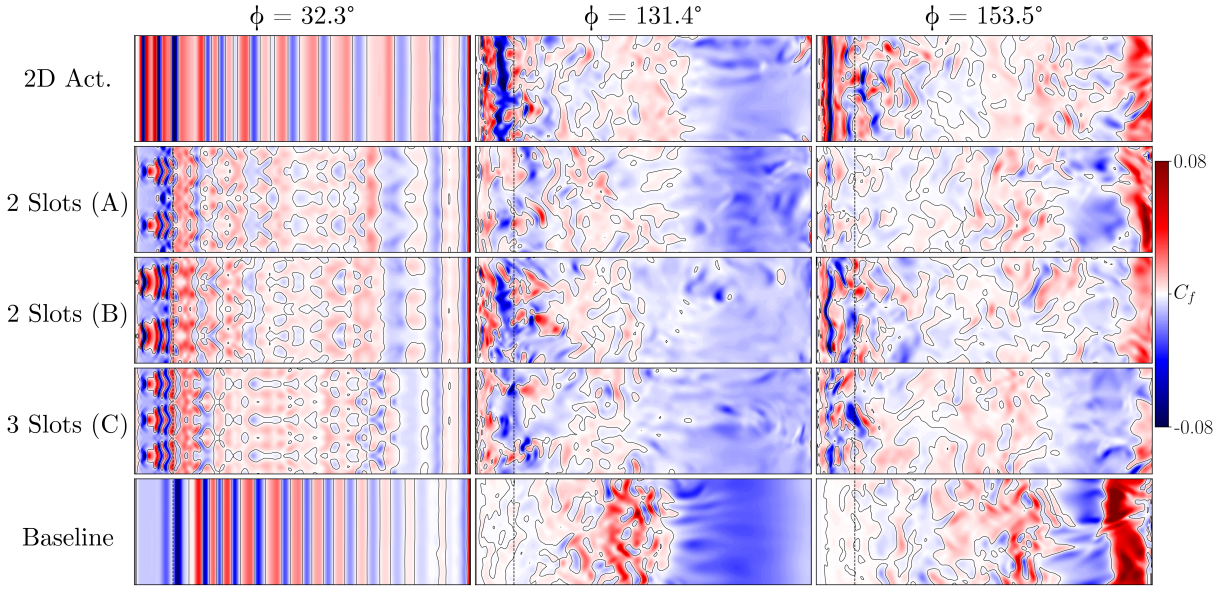

Figure 4.13: Distribution of C_f over the airfoil suction side (flow is directed from left to right) for baseline and 2D and 3D actuation with $St = 5$ (Case 2).

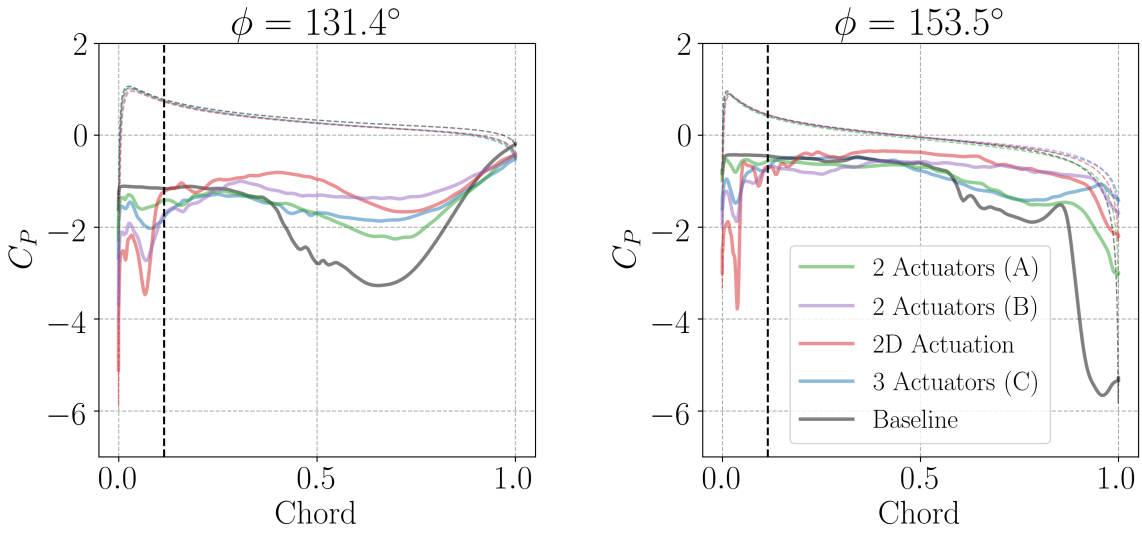

Figure 4.14: Spanwise-averaged values of C_P for different configurations of actuation with $St = 5$ (Case 2). The vertical dashed line indicates the location of x_{vsn}.

5 Flow Modal Decomposition

5.1 Formulation

5.1.1 Proper Orthogonal Decomposition

Proper orthogonal decomposition (POD) has been used in nearly every field of fluid dynamics since its introduction by Lumley (1970) and Sirovich (1987). For a review of POD and other flow modal decomposition techniques, work by Taira *et. al* (2017) is recommended. In other fields, this method is also known as principal component analysis or Karhunen–Loève expansion (Berkooz *et. al* (2003)) and it relies on singular value decomposition (SVD). The basic idea behind POD is to build an optimal set of bases that represents most of the data variance with as few basis functions as possible. To accomplish this, an SVD is performed to a covariance matrix, which is usually constructed using a kinetic energy norm. However, in this work, a pressure norm will be used instead for construction of the POD covariance matrix. Therefore, since POD searches for the most energetic modes, POD basis functions are likely to represent coherent structures with high energy content based on pressure fluctuations, as described by Holmes *et. al* (1996).

A function $\mathbf{y}$ represented on m grid points at locations $\mathbf{x}$ and time t for n snapshots can be expressed as

$$\mathbf{y}(\mathbf{x},t) = \bar{\mathbf{y}}(\mathbf{x}) + \mathbf{y}'(\mathbf{x},t) = \bar{\mathbf{y}}(\mathbf{x}) + \sum_{i=1}^{n} a_i(t)\Psi_i(\mathbf{x}) \ , \tag{5.1}$$

with $\bar{\mathbf{y}}(\mathbf{x})$ and $\mathbf{y}'(\mathbf{x},t)$ being the temporal average and fluctuations of $\mathbf{y}(\mathbf{x},t)$, respectively, Ψ being orthogonal basis eigenfunctions (spatial modes) and $\mathbf{a}(t)$ a vector that inserts temporal dynamics into the system (temporal modes). Therefore, if all modes are used after performing a proper orthogonal decomposition, all flow features are recovered.

For fluid flow simulations, spatial data (grid points) is much more abundant than temporal data (snapshots). Thus, the more memory efficient snapshot POD method Sirovich (1987) will be used. The temporal covariance between snapshots can be expressed

as

$$\langle \mathbf{y}'(\mathbf{x}, t_i), \mathbf{y}'(\mathbf{x}, t_j) \rangle = \int_V \mathbf{y}'(\mathbf{x}, t_i), \mathbf{y}'(\mathbf{x}, t_j) dV \ , \tag{5.2}$$

where V indicates the volume over which the covariance is integrated. The elements of the covariance matrix R then are given by

$$R_{i,j} = \frac{1}{n} \langle \mathbf{y}'(\mathbf{x}, t_i), \mathbf{y}'(\mathbf{x}, t_j) \rangle \ . \tag{5.3}$$

As previously stated, pressure will be used to build the covariance matrix because it allowed to recover the main behavior of aerodynamic loads with fewer modes compared to a kinetic energy norm. Performing an SVD in R provides the temporal coefficients $\mathbf{a_i} = [a_i(t_1), ..., a_i(t_n)]$ and the singular values λ_i, which are already sorted in descending order of magnitude so that the first modes are those representing most of the flow information.

To obtain the spatial modes $\mathbf{\Psi}$, a projection of snapshots onto the temporal coefficients is performed according to

$$\mathbf{\Psi_i}(\mathbf{x}) = \frac{1}{n} \sum_{j=1}^{n} a_i(t_j) \mathbf{y}'(\mathbf{x}, t_j) \ . \tag{5.4}$$

5.1.2 Spectral Proper Orthogonal Decomposition

The idea behind the spectral proper orthogonal decomposition (SPOD) proposed by Sieber *et. al* (2016) is to filter the correlation matrix R with a simple low-pass filter. The main impact of this procedure is the "cleaning" of frequency spectrum of temporal modes, what reduces noise transferring high-frequency content from lower POD modes to higher POD modes. This procedure results in a filtered correlation matrix S that can be calculated by

$$S_{i,j} = \sum_{k=-n_f}^{n_f} q_k R_{i+k,j+k} \ , \tag{5.5}$$

where n_f is the filter bandwidth and q_k are the filter coefficients. In this work, a Gaussian filter with periodic boundaries was used because of its smooth response features in time and frequency domain (Ribeiro and Wolf, 2017), being calculated according to

$$q_k = e^{-8\left(\frac{k}{n_f}\right)^2} \ . \tag{5.6}$$

All other steps follow the same procedure described in the POD formulation. The only introduced variable in this approach, when compared to the snapshot POD, is n_f which results in a classical POD when set to 0 and a discrete Fourier transform (DFT) when set to $n/2$. This property is very useful since n_f can be tuned to provide less noisy spatial and temporal bases while still keeping the main features of POD. However, one drawback is that spatial bases provided by an SPOD are not orthogonal, which can be a problem for contruction of reduced order models via Galerkin project (Carlberg *et. al*, 2011, 2013, 2017).

5.2 Results

The spectral proper orthogonal decomposition (SPOD) previously explained is performed for 3 plunging cycles (n = 1120 snapshots) of the baseline spanwise averaged data. The correlation matrix is built with pressure values at grid points and only the first 20 modes are used in reconstructions in order to investigate the fidelity for which flow features can be recovered with few modes. The domain used to perform the modal decomposition is shown in Fig. 5.1. We verified that this region provided converged results when compared to larger spatial domains.

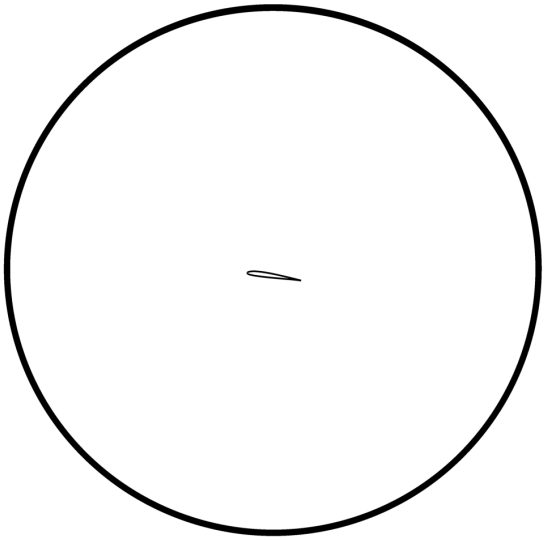

Figure 5.1: Domain used to perform flow modal decomposition. Farfield is at approximately 4.5 chords away from the airfoil.

As explained in the previous section, the size of n_f needs to be chosen by the user when decomposing the flow with SPOD. To assess the influence of this parameter, several decompositions are performed with different values of n_f as identified in Table 5.1. Figure 5.2 shows how well the flow is reconstructed using SPOD (B) with the filter bandwidth

$n_f \approx 0.25n \approx 280$. It can be seen that the main flow features are recovered at various moments, with the exception of small disturbances.

Table 5.1: Size of filter bandwidth n_f used in each modal decomposition case.

	POD	**SPOD (A)**	**SPOD (B)**	**SPOD (C)**
n_f	0	$112 \approx 0.1n$	$280 \approx 0.25n$	$449 \approx 0.4n$

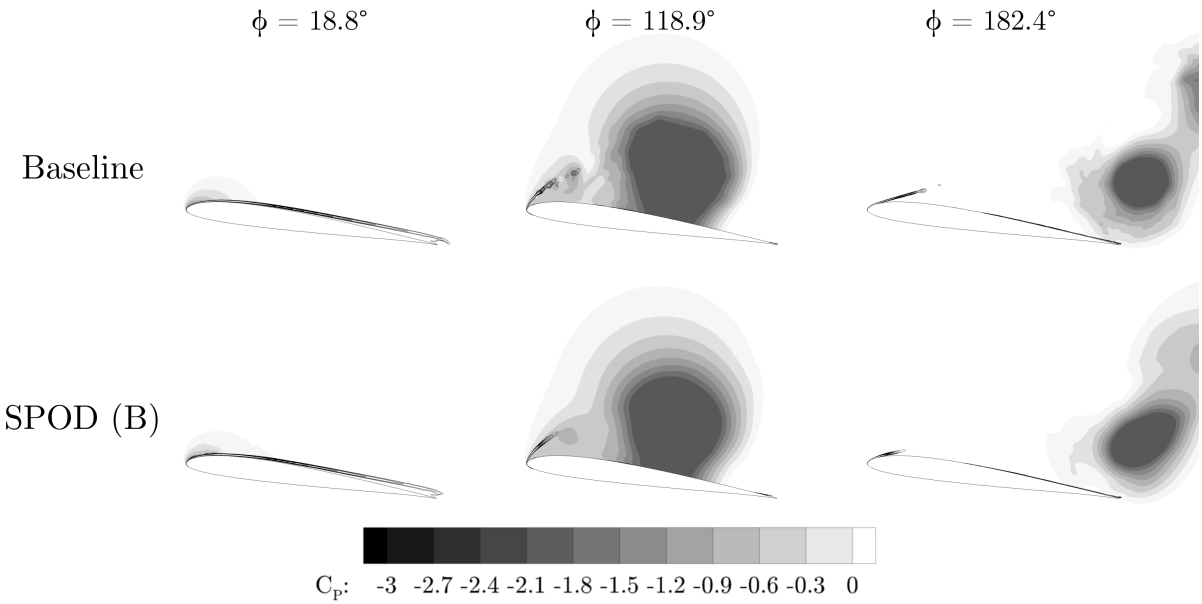

Figure 5.2: C_P contours with iso-lines of z-vorticity of spanwise-averaged baseline and SPOD (B) reconstructed flows. Decompositions performed on non-actuated flow.

Figure 5.3 shows the influence of this parameter in the calculation of aerodynamic coefficients, obtained from the (S)POD reconstructed flows. Both POD and SPOD computed with different values of n_f are able to recover fairly well the main features of the baseline flow with only 20 modes (1.79% of modes). As n_f increases, a smother, more accurate, reconstruction is obtained, especially when looking at C_D in between $300° < \phi < 10°$. That is because the flow is laminar at this stage of the plunging motion, so there are not strong pressure correlations as, for example, when the dynamic stall vortex is being transported at later moments of the plunging cycle. Therefore, a simple POD analysis is not enough to capture the flow behavior accurately for these moments.

Also, SPOD reconstructions have information of weaker modes despite having less overall information of the baseline flow. Figure 5.4a shows the normalized singular values $\bar{\lambda}_{\text{Mode}} = \frac{\lambda_{\text{Mode}}}{\sum \lambda}$ and since $\sum \lambda$ represents the total amount of information in the flow, it is possible to calculate how much information is contained in the first 20 modes, as shown in Fig. 5.4b.

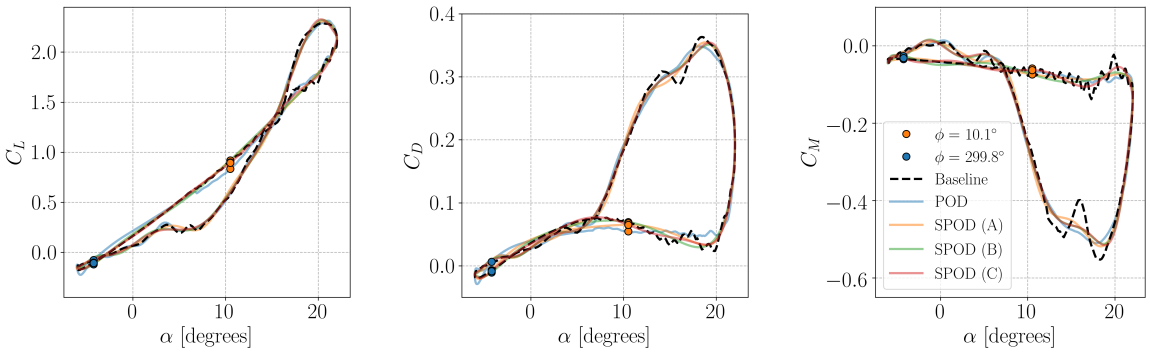

Figure 5.3: Aerodynamic coefficients from (S)POD reconstructions with different values of n_f. Here, the decompositions are performed on the non-actuated flow.

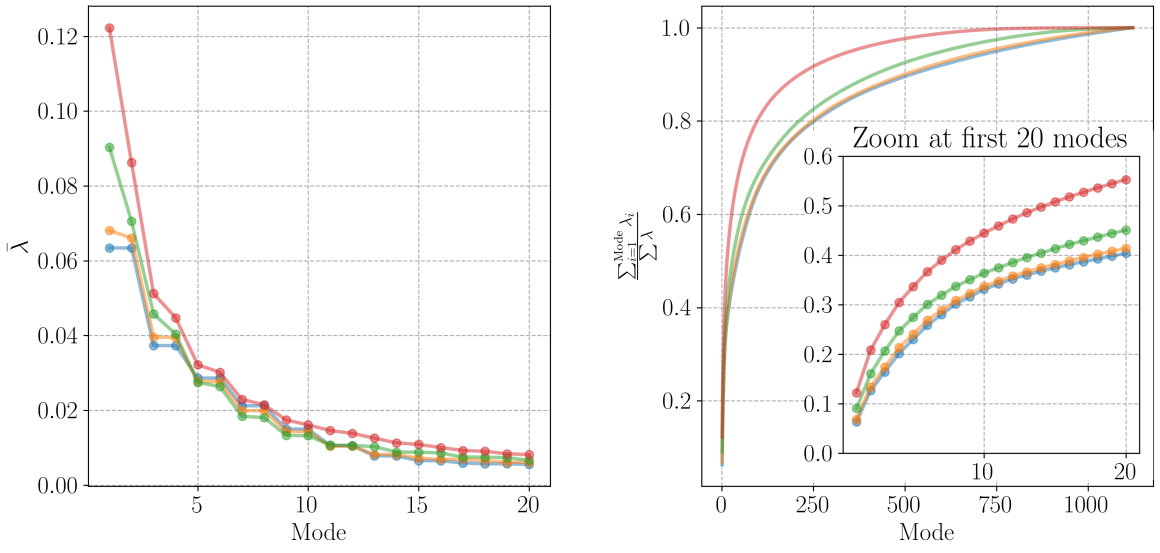

(a) (b)

Figure 5.4: Left: singular value distribution according to n_f; Right: recovered information using a certain percentage of modes. Decompositions shown are performed on the non-actuated flow.

It is clear that larger values of n_f lead to better pairing of POD the modes. Notice that the first (most energetic) modes have less information as n_f increases. When $n_f = 0$, the first 20 modes have 56.1% of the all flow information while when $n_f \approx 0.4n$ it has 40.9%. However, despite having less information, SPOD reconstructions are able to properly recover the flow as well, or even better, than POD.

Another effect of SPOD is the removal of signal noise in temporal modes as can be seen in Fig. 5.5. If n_f is too large, the shape of temporal bases is distorted and starts to become a sinusoidal signal. This effect is better seen in Fig. 5.6, which displays the dominant frequencies of each temporal mode found after performing a fast Fourier transform (FFT). It is clear that the most energetic modes are predominantly in the low frequency range and, as energy decreases, temporal bases start to have more high frequency components.

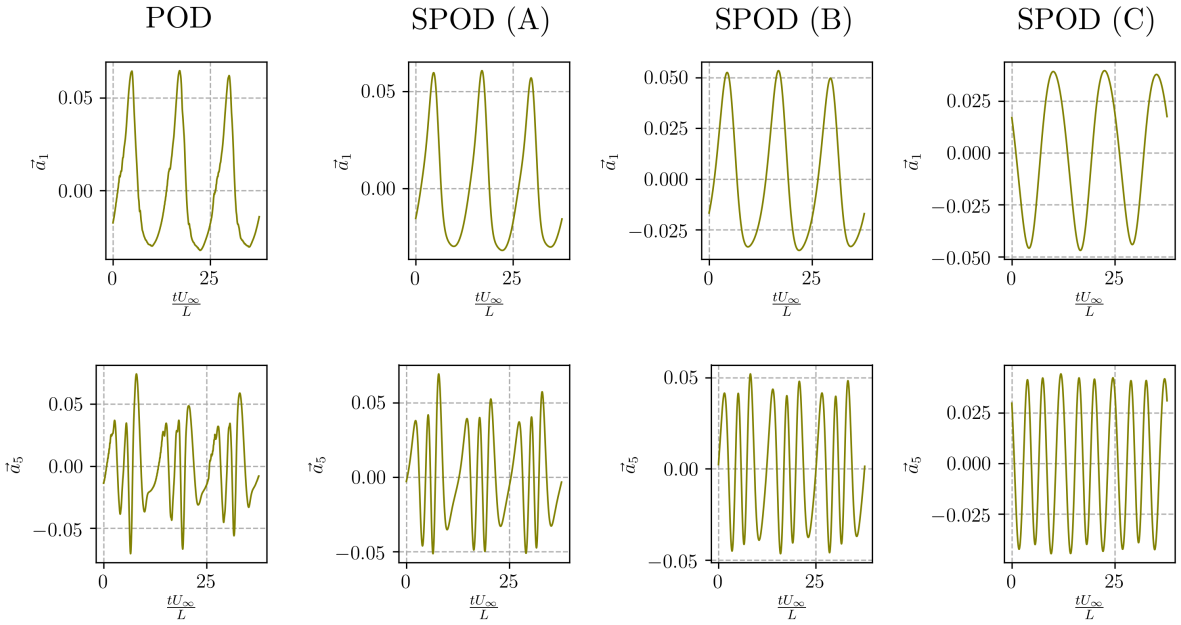

Figure 5.5: Temporal modes 1 (top row) and 5 (bottom row) for various modal decompositions performed on non-actuated flow.

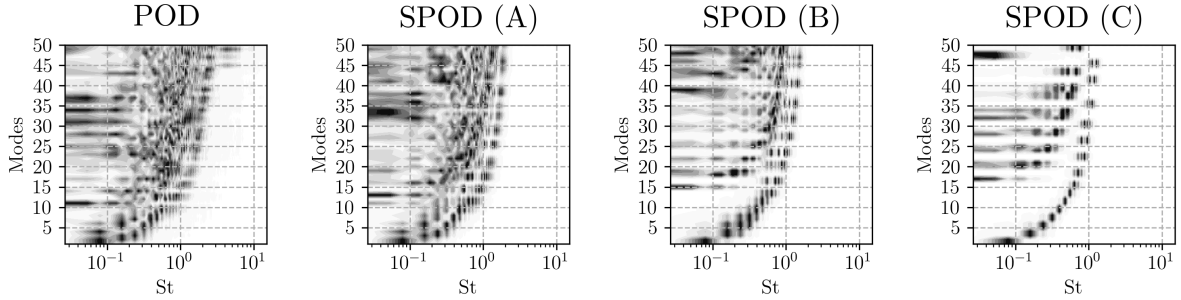

Figure 5.6: Main frequencies of temporal bases of modal decompositions performed on non-actuated flow.

Figure 5.7 shows spatial modes 1, 5 and 20 of the SPOD (B) reconstruction. The first mode is clearly associated to the dynamic stall vortex when it is at the mid-chord of

the airfoil. On the other hand, modes 5 and 20 are associated with the transport of the dynamic stall and trailing edge vortices away from the airfoil.

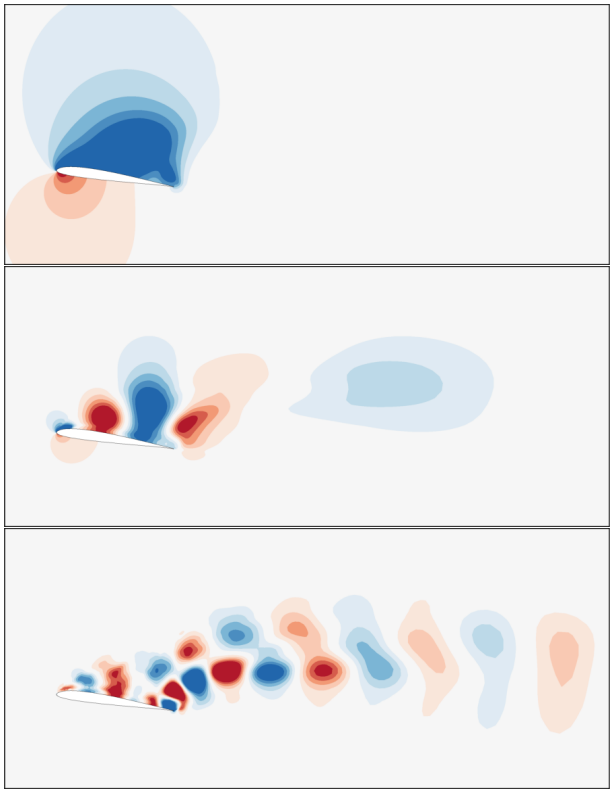

Figure 5.7: Spatial modes 1 (top), 5 (middle) and 20 (bottom) of SPOD (B) performed on non-actuated flow data.

Decomposing the flow using SPOD and a bandwidth filter with an appropriate size removes noise and does not distort temporal and spatial modes, what facilitates the construction of reduced order models. As stated before, one drawback of SPOD is the lost of orthogonality among spatial basis functions, which is a problem for reduced order models based on projection of Navier-Stokes equations. However, much progress is being made in machine learning techniques that do not require orthogonality. A recent work by Lui and Wolf (2019) used machine learning to successfully learn the behavior of temporal bases of the flow data computed in this work. This latter approach could also extrapolate the flow prediction, being able to recover all main features of the flow at later time instants.

The same flow modal decomposition methodology was also applied to data from actuated flows. Figure 5.8 shows the frequency spectrum of temporal modes of a 2D actuated flow with $St = 5$ (Case 2). One can see in this figure, specially in the map from SPOD (A), that some modes have a clear dominant frequency at $St = 5$, such as modes 9 and 10 for SPOD (A). The correspondent spatial and temporal bases of mode 9 from SPOD (A) are shown in Fig. 5.9. Since no structure similar to this was found when

decomposing the non-actuated flow, and since the dominant mode frequency is exactly that from actuation, it is safe to affirm that this structure results from flow actuation.

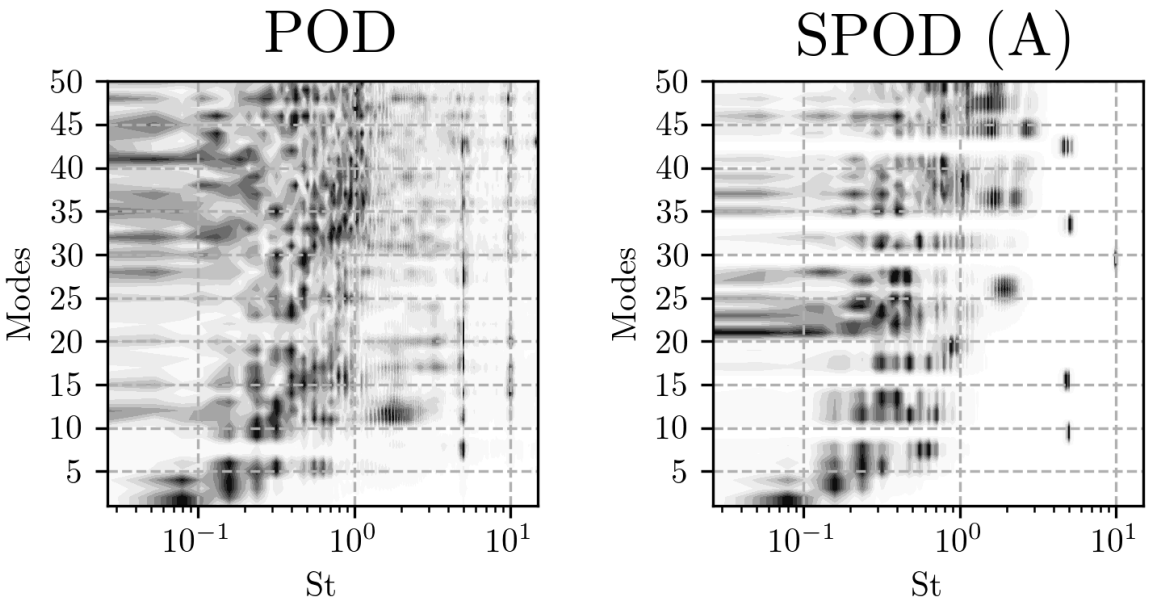

Figure 5.8: Main frequencies of POD temporal modes from a 2D actuated flow with $St = 5$ (Case 2).

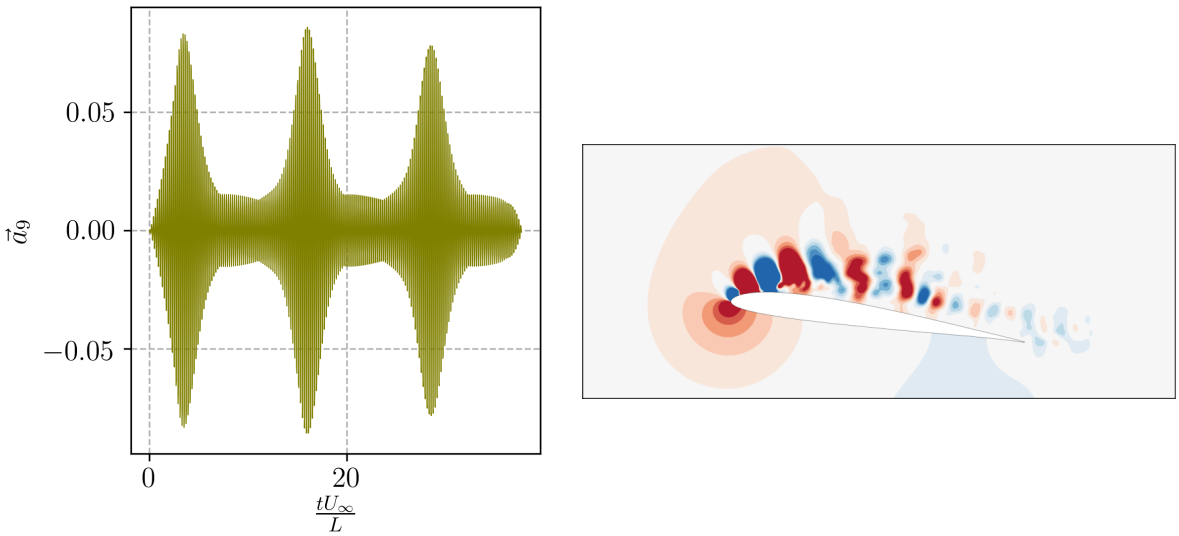

Figure 5.9: Spatial eigenfunctions (left) and temporal mode (right) 9 of SPOD (A) recovered from a 2D actuated flow with $St = 5$ (Case 2).

Despite only having data for one cycle ($n = 373$ snapshots), SPOD (A) ($n_f \approx 0.1n$) was also conducted on the data from 2D actuated flows with $St = 10$ and $St = 1$ (Case 2). To make a fair comparison, another SPOD (A) was conducted on only one cycle of the 2D actuated flow with $St = 5$ (Case 2) and for the non-actuated flow. Figure 5.10 shows that when an actuation frequency of $St = 1$ is used, there is no considerable change in

the frequency spectrum. However, for actuation frequencies of $St = 5$ and $St = 10$, these frequencies emerge in temporal modes 9 and 13, respectively, as shown in Fig. 5.11.

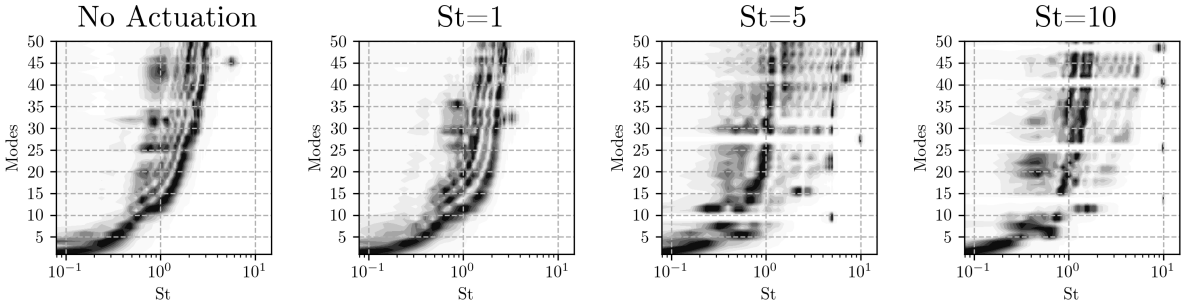

Figure 5.10: Main frequencies of temporal bases of SPOD (A) on non-actuated and 2D actuated flows with different frequencies (Case 2).

These modes have the same basic layout, despite the frequency difference, with the main part of the coherent structure being at the leading edge region. Hence, it is likely that such structures are created by actuation at this region. However, in the $St = 10$ case, the structure does not maintain its coherence until more than quarter-chord. On the other hand, for the $St = 5$ setup, coherence is maintained for a longer distance along the airfoil suction side.

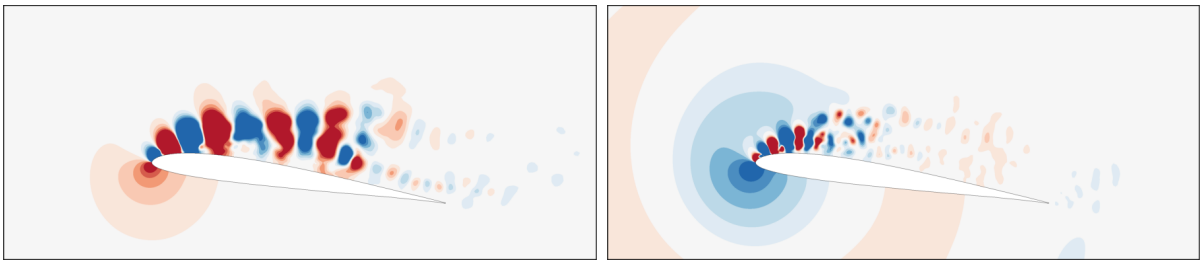

Figure 5.11: Spatial modes 9 and 13 taken from SPOD (A) of 2D actuated flow (Case 2) with $St = 5$ (left) and $St = 10$ (right).

6 Conclusions, Contributions and Recommendations

Large eddy simulations are conducted to study the flow over a SD7003 airfoil in a plunging motion. Results from the simulations are compared to data available in the literature for similar conditions and exhibit good agreement. In the current flow, instabilities arise after the beginning of the downstroke motion and a leading-edge vortex (LEV) is formed. Vorticity accumulates in the LEV, which reaches a given size, and is advected along the suction side of the airfoil increasing both lift and drag while reducing the pitching moment that induces a nose-down motion. Close to the trailing edge, the LEV is "lifted" away from the airfoil surface by a trailing-edge vortex (TEV) that forms and is also advected. As the airfoil moves upward, the flow relaminarizes. Inherent variations from cycle to cycle occur due to turbulence that develops on the airfoil suction side and, thus, four from a total of five simulated cycles are phase-averaged to calculate aerodynamic loads. In general, good agreement is found between the phase-averaged quantities and those obtained from individual cycles.

Simulations with 2D and 3D blowing and suction actuation are conducted for different frequencies which are characterized by Strouhal numbers St = 0.5 to 25. We also perform an assessment of flow actuation in terms of coefficient of momentum C_μ. Results demonstrate that actuation around St = 5 is effective in reducing both drag (C_D) and quarter-chord pitching moment coefficients (C_M) with only a mild loss in lift. For this specific frequency, it is shown that the dynamic stall vortex is broken into smaller coherent structures, leading to a pressure increase along the airfoil suction side, towards the trailing edge region. At the same time, pressure values on the suction side near the leading edge are considerably reduced, leading to a less severe lift loss and a further reduction in drag. Therefore, significant reduction in C_D and C_M are achieved as a result of mitigation of the dynamic stall vortex.

Flow configurations with 3D actuation showed that, despite being able to mitigate some of the dynamic stall vortex effects, they are not as efficient in providing a high mean lift to mean drag ratio when compared to 2D actuation. In the 3D actuated cases, transition to turbulence occurs earlier compared to 2D actuation. This effect is due to formation of three-dimensional structures which do not severely impact the disruption of the LEV, differently than the 2D actuated flow. Nevertheless, all types of 3D actuation are able to modify the LEV sufficiently such that the TEV forms farther away from the trailing edge, diminishing its impact in the overall aerodynamic loads. The present study

reveals that higher mean lift to mean drag ratios and aerodynamic damping are achieved when the actuator covers the whole airfoil span (2D actuation). Even when considering only actuators with variable spanwise widths and distribution, the most effective ones are those that cover the largest spanwise surface.

Flow modal decomposition via POD and SPOD revealed that, despite the complexity of the fluid dynamics involved in dynamic stall, 20 POD modes are sufficient to reconstruct the main flow properties fairly accurately. SPOD showed to be a great technique because of its capabilities of reducing noise in temporal modes while keeping their overall dynamics, which is a desirable feature for construction of some reduced order models. Also, POD could show coherent structures not present in the non-actuated flows but that were identified in those with actuation. The frequencies of these coherent structures had a match with the actuation frequencies. Hence, it can be concluded that they are related to actuation.

6.1 Main Accomplishments

During the course of this work, the following accomplishments were achieved:

- Implementation and validation of a 3D Navier-Stokes high order solver with the capability of simulating dynamic stall;
- Development of multiple post processing codes for statistical calculations and visualization;
- Collaboration with research group of Professor Sam Taira, including his post-doctoral researcher Dr. Chi-An Yeh (Prof. Taira is currently at University of California Los Angeles but, at the time of the research internship, his group was based at Florida State University);
- Publication and presentation of conference paper at ENCIT 2018, held in Águas de Lindóia, 2018;
- Publication and presentation of conference Paper at the AIAA SciTech, held in San Diego, 2019;
- Publication of paper on Physics Review Fluids, 2019.

6.2 Recommendations for Future Work

Due to the complexity of the dynamic stall phenomenon, there are still several remaining questions. When considering a plunging airfoil, there is still the need to have a better understanding on the impact of flow parameters such as Reynolds and Mach numbers. For example, in pitching configurations at higher Reynolds numbers, there is the appearance of a small laminar separation bubble that is responsible for triggering the dynamic stall vortex. The author is not aware of such phenomenon for plunging airfoils. For the present low Reynolds number case, the bubble does not have time to form and, this being the case, the exact mechanism that triggers the formation of the dynamic stall is not known for the current configuration. Higher Reynolds numbers may present this mechanism.

In terms of compressibility effects, transonic flows over the airfoil suction side can be reached at moderate freestream Mach numbers. In these cases, the presence of shock waves will severely impact the dynamics of the leading edge stall vortex. The present numerical tool has been tested for transonic flows and showed excellent comparisons against other tools that have high-order shock-capturing schemes implemented.

Also, for the particular flow configuration studied, 3D actuation is not as effective as 2D actuation. This was not expected, since other works show that 3D actuation often have improved effectiveness. The unknown details of the dynamic stall mechanism previously mentioned probably have something to do with such differences in actuation effectiveness. From the modal decomposition side, work still needs to me done in development of reduced order models so that less expensive simulations will be needed to search for optimal control parameters. Also, POD and SPOD are able to capture coherent structures originated from actuation that are not present in non-actuated flow data but how this can be used to design control strategies still needs to be addressed. Techniques such as dynamic mode decomposition (DMD) can be applied for the present flows to verify if the most unstable frequencies can be found for actuation. Resolvent analysis is also a promising technique that can be used for flow control and its development for airfoils undergoing prescribed motion is a challenge. Other methods of flow control can also be thought such as extremum seeking control and the OGY method.

References

ARIS, R. **Vectors, Tensors, and the Basic Equations of Fluid Mechanics**. Dover Publications, 1989.

BAIK, Y.S.; RAUSCH, J.M.; BERNAL, L.P. and OL. Experimental investigation of pitching and plunging airfoils at Reynolds number between 1 x 10^4 and 6 x 10^4. In **AIAA Paper 2009-4030**. 2009.

BEAM, R.M. and WARMING, R.F. An implicit finite-difference algorithm for hyperbolic systems in conservation-law form. **Journal of Computational Physics**, vol. 22, 87–110, 1978.

BENTON, S.I. and VISBAL, M.R. Evaluation of thermoacoustic-based forcing for control of dynamic stall. In **AIAA Paper 2018-3683**. 2018.

BERKOOZ, G.; HOLMES, P.J. and LUMLEY, J. The proper orthogonal decomposition in the analysis of turbulent flows. **Annual Review of Fluid Mechanics**, vol. 25, 539–575, 2003.

CARLBERG, K.; BARONE, M. and ANTIL, H. Galerkin v. least-squares Petrov–Galerkin projection in nonlinear model reduction. **Journal of Computational Physics**, vol. 330, 693–734, 2017.

CARLBERG, K.; BOU-MOSLEH, C. and FARHAT, C. Efficient non-linear model reduction via a least-squares petrov–galerkin projection and compressive tensor approximations. **International Journal for Numerical Methods in Engineering**, vol. 86, n. 2, 155–181, 2011.

CARLBERG, K.; FARHAT, C.; CORTIAL, J. and AMSALLEM, D. The GNAT method for nonlinear model reduction: Effective implementation and application to computational

fluid dynamics and turbulent flows. **Journal of Computational Physics**, vol. 242, 623–647, 2013.

CARR, L. Progress in analysis and prediction of dynamic stall. **Journal of Aircraft**, vol. 25, 6–17, 1988.

CARR, L.; CHANDRASEKHARA, M.; WILDER, M. and NOONAN, K. Effect of compressibility on suppression of dynamic stall using a slotted airfoil. **Journal of Aircraft**, vol. 38, n. 2, 296–309, 2001.

CHANDRASEKHARA, M.; TUNG, M. and MARTIN, P. Aerodynamic flow control using a variable droop leading edge airfoil. **AVT Specialists' Meet. Enhanc. NATO Mil. Flight Perform., Pap. RTO-MP-AVT-111**, 2004.

CHOI, H., **Turbulent Drag Reduction: Studies of Feedback Control and Flow Over Riblets**, PhD Thesis, Stanford University, 1992.

CHOUDHURI, P.G.; KNIGHT, D.D. and VISBAL, M.R. Two-dimensional unsteady leading-edge separation on a pitching airfoil. **AIAA Journal**, vol. 32, 673–681, 1994.

CORKE, T.C.; BOWLES, P.O.; HE, C. and MATLIS, E.H. Sensing and control of flow separation using plasma actuators. **Philosophical Transactions of the Royal Society A: Mathematical, Physical and Engineering Sciences**, vol. 369, n. 1940, 1459–1475, 2011.

CORKE, T.C. and THOMAS, F.O. Dynamic stall in pitching airfoils: Aerodynamic damping and compressibility effects. **Annual Review of Fluid Mechanics**, vol. 47, n. 1, 479–505, 2015.

DOMMELEN, L.L. and SHEN, S.F. The spontaneous generation of the singularity in a separating laminar boundary layer. **Journal of Computational Physics**, vol. 38, 125–140, 1980.

EKATERINARIS, J. Numerical investigations of dynamic stall active control for incompressible and compressible flows. **Journal of Aircraft**, vol. 39, n. 1, 71–78, 2002.

EKATERINARIS, J. and PLATZER, M. Computational prediction of airfoil dynamic stall. **Progress in Aerospace Sciences**, vol. 33, 759–846, 1998.

ELDREDGE, J. and JONES, A. Leading-edge vortices: Mechanics and modeling. **Annual Review of Fluid Mechanics**, vol. 51, 75–104, 2019.

FESZTY, D.; GILLIES, E. and VEZZA, M. Alleviation of airfoil dynamic stall moments via trailing-edge-flap flow control. **AIAA Journal**, vol. 42, n. 1, 17–25, 2004.

FLOREA, R. and WAKE, B. Parametric analysis of directed-synthetic jets for improved dynamic-stall performance. **41st Aerospace Sciences Meeting and Exhibit, Aerospace Sciences Meetings**, 2003.

GERONTAKOS, P. and LEE, T. Dynamic stall flow control via a trailing-edge flap. **AIAA Journal**, vol. 44, n. 3, 469–480, 2006.

GREENBLATT, D. and WYGNANSKI, I. Dynamic stall control by periodic excitation, part 1: Naca 0015 parametric study. **Journal of Aircraft**, vol. 38, n. 3, 430–438, 2001.

GREENBLATT, D.; WYGNANSKI, I.J. and RUMSEY, C.L. Aerodynamic flow control. **Encyclopedia of Aerospace Engineering**, 2010.

HAM, N.D. and YOUNG, M.I. Limit cycle torsional motion of helicopter blades due to stall. **Journal of Sound and Vibration**, vol. 4, n. 3, 431–432, 1966.

HEINE, B.; K., M.; JOUBERT, G. and RAFFEL, M. Dynamic stall control by passive disturbance generators. **AIAA Journal**, vol. 51, n. 9, 2086–2097, 2013.

HOLMES, P.; LUMLEY, J.L. and BERKOOZ, G. **Turbulence, Coherent Structures, Dynamical Systems and Symmetry**. Cambridge University Press, 1996.

JONES, K.D.; DOHRING, C.M. and PLATZER, M.F. Experimental and computational investigation of the knoller–betz effect. **AIAA Journal**, vol. 36, 1240–1246, 1998.

JOO, W.; LEE, B.S.; YEE, K. and LEE, D.H. Combining passive control method for dynamic stall control. **Journal of Aircraft**, vol. 43, n. 4, 1120–1128, 2006.

KANG, C.K.; BAIK, Y.S.; BERNAL; P., L.; V., M. and SHYY, W. Fluid dynamics of pitching and plunging airfoils for Reynolds number between 1 x 10^4 and 6 x 10^4. In **AIAA Paper 2009-536**. 2009.

LELE, S.K. Compact finite difference schemes with spectral-like resolution. **Journal of Computational Physics**, vol. 103, 16–42, 1992.

LOMBARDI, A.; BOWLES, P. and CORKE, T. Closed-loop dynamic stall control using a plasma actuator. **AIAA Journal**, vol. 51, n. 5, 1130–1141, 2013.

LORBER, P.; MCCORMICK, D.; ANDERSON, T.; WAKE, B.; MACMARTIN, D.; POLLACK, M.; CORKE, T. and BREUER, K. Rotorcraft retreating blade stall control. In **AIAA Paper 2000-2475**. 2000.

LUI, H.F.S. and WOLF, W.R. Construction of reduced-order models for fluid flows using deep feedforward neural networks. **Journal of Fluid Mechanics**, vol. 872, 963–994, 2019.

LUMLEY, J.L. **Stochastic Tools in Turbulence**, vol. 12. Dover Publications, 1970.

MARTIN, P.; WILSON, J.; BERRY, J.; WONG, T.; MOULTON, M. and MCVEIGH, M. Passive control of compressible dynamic stall. In **AIAA Paper 2008-7506**. 2008.

MCCROSKEY, W. **The phenomenon of dynamic stall**. Defense Technical Information Center, 1981.

MCCROSKEY, W.J. Unsteady airfoils. **Annual Review of Fluid Mechanics**, vol. 14, 285–311, 1982.

MUNDAY, P. and TAIRA, K. Effects of wall-normal and angular momentum injections in airfoil separation control. **AIAA Journal**, vol. 56, 1830–1842, 2018.

NAGARAJAN, S., **Leading Edge Effects in Bypass Transition**, PhD Thesis, Stanford University, 2004.

OL, V.M.; BERNAL, L.P.; KANG, C.K. and SHYY, W. Shallow and deep dynamic stall for flapping low Reynolds number airfoils. **Experiments in Fluids**, vol. 46, 883–901, 2009.

ORLANDI, P. A numerical method for direct simulation of turbulence in complex geometries. **CTR Annual Research Briefs**, p. 215–229, 1989.

POST, M.L. and CORKE, T.C. Separation control using plasma actuators: Dynamic stall vortex control on oscillating airfoil. **AIAA Journal**, vol. 44, n. 12, 3125–3135, 2006.

RADESPIEL, R.; WINDTE, J. and SCHOLZ, U. Numerical and experimental flow analysis of moving airfoils with laminar separation bubbles. **AIAA Journal**, vol. 45, 1346–1356, 2007.

RAMOS, B.L.O. Pressure coefficient. 2019a.
URL: *https://youtu.be/XZ6bKbQ5Olw*

RAMOS, B.L.O. Pressure coefficient contours at airfoil suction side. 2019b.
URL: *https://youtu.be/BcPTLfVt5Gs*

RAMOS, B.L.O. Q-criterion colored by pressure coefficient. 2019c.
URL: *https://youtu.be/TyqTUFLx-1w*

RAMOS, B.L.O. Skin friction contours at airfoil suction side. 2019d.
URL: *https://youtu.be/e-gzAoSjRkg*

RAMOS, B.L.O. Z-vorticity. 2019e.
URL: *https://youtu.be/0cxoxqZHvUk*

RIBEIRO, J.H.M. and WOLF, W.R. Identification of coherent structures in the flow past a Naca0012 airfoil via proper orthogonal decomposition. **Physics of Fluids**, vol. 29, 085104, 2017.

SIEBER, M.; PASCHEREIT, C.O. and OBERLEITHNER, K. Spectral proper orthogonal decomposition. **Journal of Fluid Mechanics**, vol. 792, 798–828, 2016.

SIROVICH, L. Turbulence and the dynamics of coherent structures part I: Coherent structures. **Quarterly of Applied Mathematics**, vol. 45, n. 3, 561–571, 1987.

SUN, M. and SHEIKH, S.R. Dynamic stall suppression on an oscillating airfoil by steady and unsteady tangential blowing. **Aerospace Science and Technology**, vol. 3, n. 6, 355–366, 1999.

TAIRA, K.; BRUNTON, S.L.; DAWSON, S.T.M.; ROWLEY, C.W.; COLONIUS, T.; MCKEON, B.J.; SCHMIDT, O.T.; GORDEYEV, S.; THEOFILIS, V. and UKEILEY, L.S. Modal analysis of fluid flows: An overview. **AIAA Journal**, vol. 55, n. 12, 4013–4041, 2017.

TRAUB, L.; MILLER, A. and REDINIOTIS, O. Effects of active and passive flow control on dynamic stall vortex formation. **Journal of Aircraft**, vol. 41, n. 2, 405–408, 2004.

VISBAL, M. and BENTON, S. Exploration of high-frequency control of dynamic stall using large-eddy simulations. **AIAA Journal**, vol. 56, n. 8, 2974–2991, 2018.

VISBAL, M.R. Dynamic stall of a constant-rate pitching airfoil. **Journal of Aircraft**, vol. 27, 400–407, 1990.

VISBAL, M.R. On the formation and control of the dynamic stall vortex on a pitching airfoil. In **AIAA Paper 1991-6**. 1991.

VISBAL, M.R. Numerical investigation of deep dynamic stall of a plunging airfoil. **AIAA Journal**, vol. 49, 2152–2170, 2011.

VISBAL, M.R. Numerical exploration of flow control for delay of dynamic stall on a pitching airfoil. In **AIAA Paper 2014-2044**. 2014.

VISBAL, M.R. Control of dynamic stall on a pitching airfoil using high-frequency actuation. In **AIAA Paper 2015-1267**. 2015.

VISBAL, M.R. and GARMANN, D.J. Control of dynamic stall over a pitching finite-aspect-ratio wing. In **AIAA Paper 2017-4118**. 2017.

VISBAL, M.R. and SHANG, J.S. Investigation of the flow structure around a rapidly pitching airfoil. **AIAA Journal**, vol. 27, 1044–1051, 1989.

WARSI, Z.U.A.; DEVARAYALU, K. and THOMPSON, J.F. Numerical solution of the Navier-Stokes equations for arbitrary blunt bodies in supersonic flows. **Numerical Heat Transfer**, vol. 1, 499–516, 1978.

WEAVER, D.; MCALISTER, K.W. and TSO, J. Control of vr7 dynamic stall by strong steady blowing. **Journal of Aircraft**, vol. 41, n. 6, 1404–1413, 2004.

YAMAMOTO, S. and DAIGUJI, H. A numerical method for the transonic cascade flow problem. **Computers and Fluids**, vol. 19, 461–477, 2001.

YANG, Z. and VOKE. Large-eddy simulation of boundary-layer separation and transition at a change of surface curvature. **Journal of Fluid Mechanics**, vol. 439, 305–333, 2001.

YEH, C. and TAIRA, K. Resolvent-analysis-based design of airfoil separation control. **Journal of Fluid Mechanics**, vol. 867, 572–610, 2019.